Sensitivity analysis of inverted model parameters from transient electromagnetic measurements affected by induced polarization effects

Aigner, Lukas; Werthmüller, Dieter; Flores Orozco, Adrián

Important note
To cite this publication, please use the final published version (if applicable).
Please check the document version above.

Sensitivity analysis of inverted model parameters from transient electromagnetic measurements affected by induced polarization effects

Lukas Aigner [a,*], Dieter Werthmüller [b], Adrián Flores Orozco [a]

[a] *Research Unit Geophysics, Department of Geodesy and Geoinformation, TU Wien, Vienna, Austria*
[b] *Applied Geophysics and Petrophysics, Faculty of Civil Engineering and Geosciences, TU Delft, Delft, the Netherlands*

ARTICLE INFO

ABSTRACT

We investigate the application of the distance-based global sensitivity analysis (DGSA) to evaluate the sensitivity of electrical model parameters obtained from transient electromagnetic (TEM) data including induced polarization (IP) effects. We propose novel open-source forward modeling and inversion routines for single-loop TEM data including IP effects with the maximum phase angle model to model the frequency dependence of the complex resistivity. In a first step, we evaluate the accuracy of our forward modeling and inversion routines using numerical studies, where the actual variations of layer thicknesses and resistivities, as well as the frequency dependence of the complex resistivity is known. In a second step, we extend our investigation to field data and apply our approach to three distinct case studies in layered media: 1) a confined aquifer corresponding to conductive non-polarizable media, 2) a graphite deposit corresponding to highly conductive and polarizable anomalies in a resistive host rock and 3) an ice glacier corresponding to highly resistive polarizable media. Our DGSA results reveal that standard depth of investigation (DOI) approaches may overestimate the true sensitivity of the model obtained from the inversion. TEM data collected in conductive layered media without IP effects show reduced sensitivity above the predicted DOI. The case studies in polarizable media demonstrate that the maximum phase angle is more influential on the TEM model response than the relaxation time and dispersion coefficient. Our DGSA results for polarizable media reveal that TEM field data collected at the graphite deposit and at the ice glacier are sensitive to the geometry of the polarizable layer.

1. Introduction

The transient electromagnetic (TEM) method derives variations of the electrical resistivity from the diffusion of eddy currents in the subsurface. The TEM method uses a loop antenna at the surface to measure induced voltage readings that typically have a positive sign and decay smoothly over time. Weidelt (1982) has demonstrated that negative voltage readings can be measured, but are only physically plausible if the electrical resistivity of the subsurface is frequency dependent, i.e., in presence of polarizable media (Smith and West, 1988). This is commonly referred to as induced polarization (IP) effects, which have been documented in transient electromagnetic (TEM) measurements since the late 1970s (e.g., Lee, 1975; Spies, 1980). Modeling and inversion of TEM data obtained over chargeable subsurface materials without taking IP effects into account leads consequently to an erroneous electrical subsurface model as demonstrated for example by Viezzoli and Manca (2020) and Grombacher et al. (2021). Due to the

common usage of TEM surveys in ore exploration, most studies have reported IP effects in TEM data measured on conductive subsurface media (e.g., Flores and Peralta-Ortega, 2009; Zeng et al., 2019; Kang et al., 2020; Maurya et al., 2022). However, recent studies have also reported IP effects in resistive media associated to frozen ground (e.g., Kozhevnikov and Antonov, 2012; Grombacher et al., 2021).

Maurya et al., 2022 demonstrated that an improved hydrogeological interpretation of an extensive TEM data set is possible when taking IP effects into account. The authors use the tTEM system which employs an offset loop configuration (i.e., separated transmitter and receiver loops) and invert the TEM data with a lateral constraint inversion approach (e.g., Auken and Christiansen, 2004; Lin et al., 2019) that is part of a commercial software package (Auken et al., 2015). While the tTEM system allows for rapid data acquisition and a depth of investigation up to 100 m, its deployment is limited in sites that the ATV can not reach such as rough terrain and steep slopes (e.g., high altitude mountain areas). IP effects have also been reported in airborne TEM data (e.g.,

---

* Corresponding author.
  E-mail address: lukas.aigner@geo.tuwien.ac.at (L. Aigner).

Grombacher et al., 2021; Kang et al., 2020; Lin et al., 2019). While airborne TEM systems can cover large areas efficiently, they might not be suited for small-scale surveys such as alpine permafrost sites.

The modeling of IP effects in TEM data requires to account for the complex resistivity and its frequency dependence. Pelton et al. (1978) described the frequency dependence of the complex electrical resistivity with a mathematical dispersion model (Pelton Model, PM), which has been applied by, e.g., Flores and Peralta-Ortega (2009) and Seidel and Tezkan (2017) to model IP effects in 1D. Kang and Oldenburg (2016) use a full 3D modeling approach in the SimPEG framework (Cockett et al., 2015; Heagy et al., 2017) and model the IP effects with the PM. The modeling of TEM responses including the frequency dependence of the complex resistivity requires three additional model parameters per layer, namely chargeability, relaxation time and dispersion coefficient. This drastically increases the non-uniqueness of the inverse problem compared to only two parameters per layer (i.e., DC resistivity and thickness) for modeling TEM data without IP effects. Bérubé et al. (2017) and Madsen et al. (2017) have both observed a correlation between the chargeability and dispersion coefficient in low frequency IP measurements with electrical methods. Therefore, Fiandaca et al. (2018) introduced a re-parameterization of the PM, the so-called maximum phase angle (MPA) model, which replaces the chargeability with the maximum phase angle ($\phi_{\max}$) of the complex resistivity. Lin et al. (2019) have shown that the MPA model also helps to reduce the correlation between parameters in the case of TEM data leading to an improved parameter estimation in the inversion of TEM soundings with IP effects.

The use of the depth of investigation (DOI) obtained from the Jacobian matrix of the final model from a deterministic inversion approach (e.g., Christiansen and Auken, 2012; Fiandaca et al., 2015) is the standard method to investigate to which depth the inverted model is sensitive to the data. The DOI, however, does not provide information on the reliability of individual model parameters (e.g., the thickness and resistivity of each layer) after the inversion. Alternative methods, such as the distance-based global sensitivity analysis (DGSA, Fenwick et al., 2014) are capable of investigating multidimensional model responses, such as time series, estimating the sensitivity of each individual model parameter from a given uniform prior distribution of models. The DGSA is computationally more expensive than the DOI estimation, because it requires ca. 1000s of forward model calculations and the statistical analysis of their distribution in different clusters. Most studies have applied the DGSA to reservoir modeling (e.g., Fenwick et al., 2014) or reactive transport modeling (e.g., Perzan et al., 2021), which highlight the capability of the DGSA to obtain the sensitivity of the model parameters for large and complex models. Recently, Hermans et al. (2018) quantified the sensitivity of heat transport while monitoring with the electrical resistivity tomography and Michel et al. (2020) applied the DGSA for surface nuclear magnetic resonance measurements.

The objective of this work is to investigate the applicability of the DGSA method to quantify the influence of 1D model parameters on the model response. To this end, we adapt existing open-source Python libraries that permit the forward modeling and deterministic inversion of TEM data including IP effects. We evaluate the resolution of our forward modeler through the comparison of responses obtained with commercial software and open-source libraries, whereas the accuracy of our inversion is evaluated in a numerical study. We present the application of our 1D TEM modeling and inversion routines in three distinct case studies: (1) a gravel aquifer related to conductive media without IP effects, (2) a graphite ore deposit related to conductive media with IP effects and (3) an ice glacier related to resistive media with IP effects. To the best of our knowledge, this study offers the first application of the DGSA to estimate the sensitivities of TEM model parameters including IP effects.

We investigate the application of the proposed methodology for the modeling and inversion of TEM data in a single-loop configuration. Recently, Bücker et al. (2021) and Aigner et al. (2021) have demonstrated its applicability and its simplified field procedures for waterborne measurements. Hence, single-loop configurations, as explored here, offer a suitable alternative for investigations of alpine permafrost sites and other regions with difficult terrain. Our approach can be easily implemented for other TEM instruments and configurations because we use open-source libraries as described in detail in the next section.

2. Material and methods

2.1. TEM measurement principle and forward modeling

The TEM method is based on injecting a direct current in a horizontal square loop antenna to measure the changes of electrical resistivity of the subsurface. The injected current is interrupted causing a primary magnetic field to decay over time which induces eddy currents into the ground. The eddy currents diffuse downward and laterally into the subsurface over time generating a secondary magnetic field (e.g., Nabighian, 1979). The temporal change of the secondary magnetic field can be measured as a voltage-decay induced into a receiver loop antenna at the surface. The shape and rate of voltage decay depends on the electrical resistivity (ρ) of the subsurface. The voltage readings have typically a positive sign as long as the subsurface resistivity is independent of frequency. In presence of polarizable media in the subsurface, the dispersion of the electrical resistivity may cause continuous sign-reversals of the voltage readings (Weidelt, 1982). Such sign reversals may also be caused by a high conductivity contrast between conductive ore material and host rock as shown by Li et al. (2017). Further details on the TEM method can be found in Telford et al., 1990, Nabighian et al., 1991 and Christiansen et al., 2006.

We developed a forward modeler that can reproduce the signal responses generated with the TEM-FAST system (manufactured by AEMR - Applied Electromagnetic Research, Utrecht, the Netherlands) using functions available in the open source library empymod by Werthmüller (2017). The algorithms of empymod model the full 3D EM wavefield based on a vertical transversal isotropic (VTI) distribution of subsurface electrical resistivity. The calculations in the wavenumber-frequency domain are based upon the work by Hunziker et al., 2015 and the necessary Hankel and Fourier transformation algorithms to obtain the EM fields in space-frequency and space-time domain are based upon Key, 2012. We model the TEM-FAST system in a single-loop configuration with empymod by implementing the system parameters (see Table A1 of Appendix A.1) and set the shape of the current pulse based upon the chosen measurement settings as well as the turn-off ramp measurements (see Table A2 of Appendix A.1). We then model the TEM response, i.e., decay curve at the required time gates, for a square transmitter loop under the diffusive approximation to obtain the resulting vertical magnetic field in the center of the loop. The modeling is done in the wavenumber-frequency domain by using digital linear filters (DLF) for the required Hankel and Fourier transforms to obtain the response in the space-time domain (see Werthmüller et al., 2019). When including IP effects, we use the 601 point cosine-sine DLF for the Fourier transformation and the 401 point DLF for the Hankel transformation (both from Key, 2009) to obtain a smooth TEM response. We use a first-order, butterworth low-pass filter (Butterworth, 1930) with a cut-off frequency of 10^8 Hz to remove high frequency noise from the TEM model response that is caused by the near-singular behaviour of the derivation of the Maxwell Equations in the wavenumber-frequency domain. For a comparison of our implementation of the TEM forward model in a single-loop configuration to other algorithms please see the complementary material in Appendix A.2.

The frequency dependence of the complex electrical resistivity was modelled with the dispersion model proposed by Pelton et al. (1978) that can be written as:

$$\rho(\omega) = \rho_0 \left[1 - M \left(1 - \frac{1}{1 + (i\omega\tau)^c} \right) \right],\tag{1}$$

where ω is the angular frequency, ρ_0 denotes the DC resistivity, M the

chargeability, τ the relaxation time and c the dispersion coefficient. We use M to represent the chargeability (instead of m as commonly used in the literature) to avoid confusions with the model parameter vector (m) used in the inversion, as described in the next subsection. To overcome the increased non-uniqueness in the inversion of TEM data including IP effects, Lin et al. (2019) suggests the use of: 1) robust starting models, 2) constraining the relaxation time and dispersion coefficient in the first few iterations, 3) increased error of readings close to the sign change 4) modified damping scheme and 5) re-parameterization of the model space to reduce the correlation between the chargeability and the dispersion coefficient. In our study we use only 3 of the 5 suggested improvements, namely: Robust starting model to facilitate convergence of the inversion, an increased error close to the sign change for field data and a re-parameterization of the model space. In particular, we use the maximum phase angle model (MPA), a re-parameterized version of Eq. (1) proposed by Fiandaca et al. (2018). The chargeability M is replaced by ϕ_{max} which is the maximum phase angle of the complex resistivity and τ with τ_ϕ which equals the frequency $1/(2\pi\tau_\phi)$ at which ϕ_{max} is observed. The parameters τ and τ_ϕ are directly related by $\tau_\phi = \tau(1 - M)^{(1/2c)}$ and ϕ_{max} can be calculated from the classical Pelton model parameters using (Fiandaca et al., 2018):

$$\phi_{max} = -tan^{-1}\left(\frac{\rho^{''}\left(1/\tau_\phi\right)}{\rho^{'}\left(1/\tau_\phi\right)}\right). \tag{2}$$

2.2. Deterministic inversion algorithm

We conduct the deterministic inversion of TEM data including IP effects using our proposed forward modeler and the open-source library pyGIMLi (Rücker et al., 2017). We use a block inversion scheme where the layer thicknesses, the electrical resistivity and the MPA model parameters can be independently varied for media with and without IP effects. The block inversion scheme is based upon a Marquardt-type damped Gauss-Newton scheme (Marquardt, 1963; Inman, 1975), which minimizes the following objective function (adapted from Wagner et al., 2019):

$$\|W_d(d - \mathscr{F}(m))\|_2^2 + \lambda^2\|W_m m\|_2^2 + \kappa^2\|W_c(m - m_0)\|_2^2 \rightarrow min. \tag{3}$$

The first term contains the misfit between the forward response $\mathscr{F}(m)$ and the data vector d in terms of voltage readings at the selected time gates in V/m^2. The misfit is weighted with the inverse of the absolute error estimates W_d, which are also given in V/m^2. The second term contains the regularization parameter λ applied to the model vector m using the matrix W_m that holds the first-order roughness operators to facilitate smoothness in the model parameters. In the case of media without IP effects the model vector m contains the thickness and resistivity for each layer of the subsurface model, whereas in the case of media with IP effects m will additionally contain the MPA model parameters. The third term introduces a damping regularization to incorporate prior information into m by penalizing deviations from selected initial model parameters m_0. Model parameters of m that will be fixed close to their initial value are selected through the i and j elements of the W_c matrix. The number of rows (i) equals the number of parameters that should be constrained, while the number of columns (j) equals the total number of model parameters. Entries in W_c that equal one mark the positions of the constrained model parameters within the model vector (e.g., if the entry n is one, it will constrain the model to the initial value of parameter n) and each row can only have one entry as one, whereas all the other entries must remain zero. Since TEM data with IP effects may contain negative voltage readings, we use the data vector d directly in V/m^2, without any transformation, whereas we use a logarithmic transformation in the case of TEM data without IP effects as well as for all model parameters m.

The block inversion scheme is obtained by using a Marquardt-type inversion approach that uses a successive cooling of the regularization

parameter λ with a damping factor β (Günther and Müller-Petke, 2012). For example, a choice of $\beta = 0.8$ reduces λ in successive inversion steps by 20% until the inversion converges. We minimize the objective function (Eq. (3)) by solving the following system of normal equations for the model parameter update δm in a least-squares sense with the algorithm "LSQR" by Paige and Saunders (1982), following the implementation by Wagner et al. (2019):

$$\begin{bmatrix} W_d\widehat{J} \\ \lambda W_m \\ \kappa\widehat{W}_d \end{bmatrix}\delta m = \begin{bmatrix} W_d(d - \mathscr{F}(m)) \\ -\lambda W_m m \\ \kappa(m_0 - \widehat{W}_c m) \end{bmatrix}, \tag{4}$$

with $\widehat{W}_c = W_c diag(\partial m/\partial p)^{-1}$ and the Jacobian matrix $\widehat{J} = J diag(\partial m/\partial p)^{-1}$. We fill J using a numerical finite-difference approach (part of the pyGIMLi modeling framework), which repeatedly calculates the forward response with slightly perturbed model parameters. We formulate three different stopping criteria for the inversion: (1) reaching the maximum of twenty five iterations, (2) reaching a weighted root-mean-square error (referred to as χ^2) of the data misfit ≤ 1, or (3) when the misfit of consecutive iteration differs by less than 2%. Furthermore, we use both the relative root-mean-square error (rRMSE) and the χ^2 error to quantify the accuracy of our data fit and details on their computation are presented in Appendix A.3).

We calculate the DOI following the classical skin-depth approach by Spies (1989), which can be calculated following Yogeshwar et al. (2020):

$$DOI \approx 0.55\left(\frac{M_m \cdot \bar{\rho}}{\eta}\right), \tag{5}$$

where M_m denotes the magnetic moment of the transmitter loop, which is equal to $I \cdot A_{Tx} \cdot n$ with A_{Tx} being the transmitter area, I the injected current and n the number of turns of the transmitter loop. The noise level (η) is approximated by the measured voltage of the last time gate (after filtering) and $\bar{\rho}$ is the average resistivity of the inversion result (Yogeshwar et al., 2020):

$$\bar{\rho} = \frac{1}{DOI}\int_{z=0}^{DOI} \rho(z)dz, \tag{6}$$

with $\rho(z)$ being the inverted resistivity at a certain depth z.

2.3. Distance-based global sensitivity analysis

We use the distance-based global sensitivity analysis (DGSA) approach proposed by Fenwick et al. (2014) that is based upon the seminal work of Spear and Hornberger (1980). We forward calculate n TEM responses for layered media with a constant number of layers, where each layer is defined by its thickness, ρ_0 as well as ϕ_{max}, τ_ϕ and c (the last three only for polarizable layers). We then classify the responses into k clusters based on Euclidean distances between the responses and calculate cumulative density functions (CDF) for the empirical distribution function (from sampling) of the prior distribution $\widehat{F}(p_i)$ and the k class-conditional empirical distribution functions $\widehat{F}(p_i|c_k)$. The measure of sensitivity for parameter p_i is calculated as the area between the CDFs $\widehat{F}(p_i)$ and $\widehat{F}(p_i|c_k)$ (commonly denoted as CDF distance Δ_{cdf}). In the case of $k > 2$ classes the sensitivity is typically calculated as the average of the individual Δ_{cdf}.

We use the pyDGSA library (Perzan et al., 2021) and create the uniformly distributed model realizations using a Saltelli sampler (e.g., Saltelli et al., 2008) that is part of the SALib library (Herman and Usher, 2017; Iwanaga et al., 2022). We determine a prior range from a given initial model for each model parameter (i.e., thickness, ρ_0, ϕ_{max}, τ_ϕ and c) with a minimum and maximum that is equal to 1/4 and 4 times of the model parameter value obtained from the inversion. To avoid physically implausible prior ranges in ϕ_{max} and c, we set the upper boundary to a

maximum of 1.0 in cases where 4 times the parameter value exceeds 1. We ensure full coverage of the specified prior range, by employing a sampling approach that increases the number of models for increased number of parameters in the mean model, resulting in a number of samples between 10,000 and 40,000. In case of layered media exhibiting IP effects, we exclude models where $\phi_{max} = 0$. We then calculate the corresponding forward responses only for the remaining models. Those forward responses are classified into k different clusters with k-medoids clustering, while the optimal number of clusters was determined using the Silhouette score by Rousseeuw (1987). The DGSA methodology requires additional computational time that mainly depends on the number of forward models that are simulated as well as on the number

of clusters that are investigated. The DGSA experiments in our study required approximately an additional hour after the inversion was finished when using 20,000 forward model runs.

3. Case studies: numerical and field data

To evaluate the proposed inversion methodology of TEM data including IP effects, we conducted numerical and field data experiments related to three different study sites in Austria (see Fig. 1). Site one is related to intercalations of clay and sandy gravel layers that correspond to variations in resistivity without IP effects (Fig. 1b). Site two is related to a former graphite mine (Fig. 1d) that corresponds to media with low
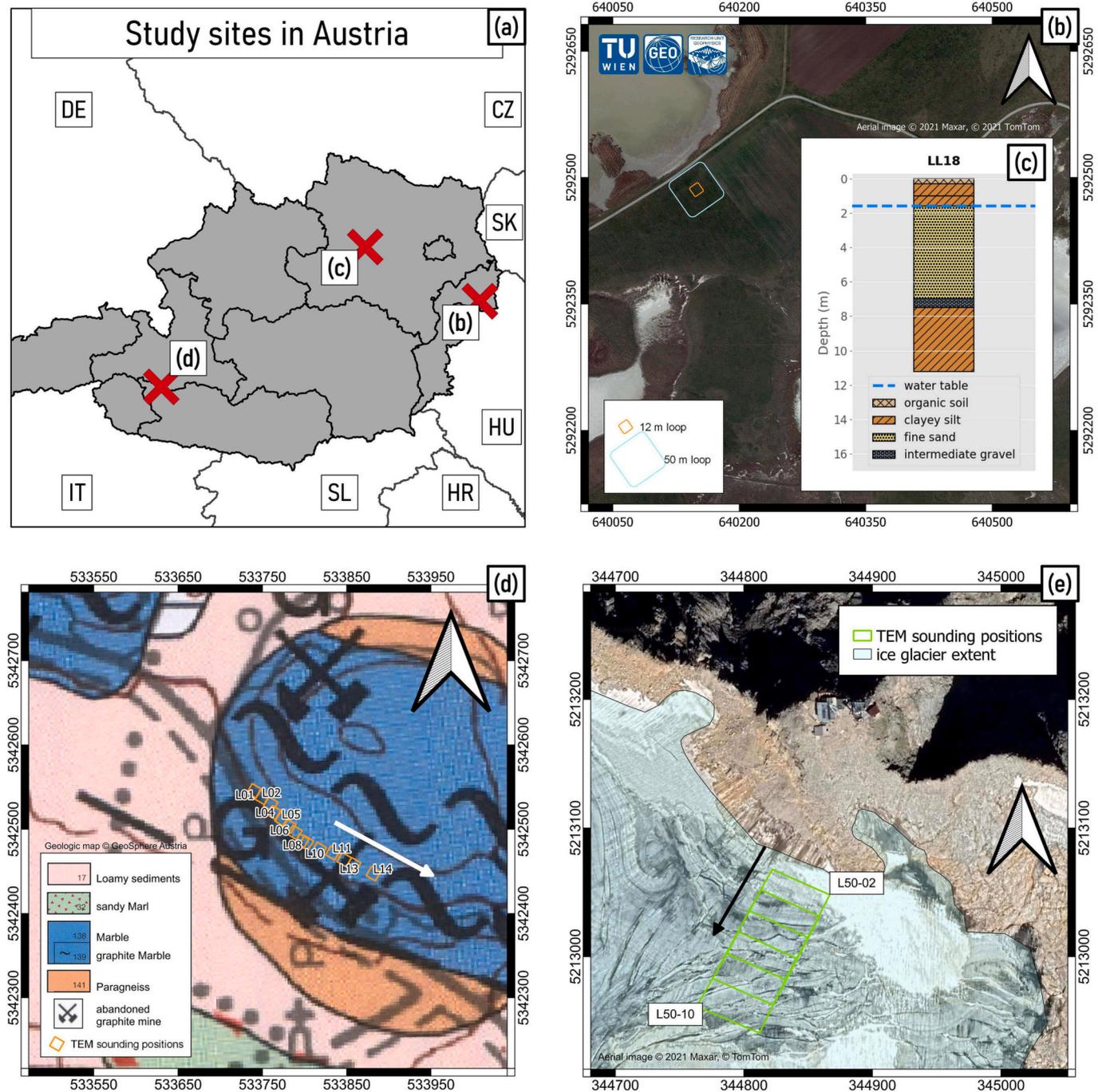
Fig. 1. Panel (a) shows the locations of the study sites within Austria and in relation to its neighboring countries. Panel (b) shows the position of the TEM soundings at the soda lakes test site including stratigraphic information acquired from a borehole (sub-panel c). Panel (d) shows the TEM profile imposed on a geological map of the study site. Panel (e) shows the positions of the TEM soundings at the ice glacier near the peak of Hoher Sonnblick in relation to the extent of the ice glacier.

electrical resistivity and high polarization. Site three is related to an alpine ice glacier (Fig. 1e) that corresponds to high resistivity and is also polarizable due to the presence of ice. Due to limited availability of ground truth data an interpretation of our inversion results in terms of graphite and ice content is beyond the scope of this study.

The numerical model associated to the first site is based on conductive, non-polarizing media consisting of two sandy gravel aquifers confined in clay rich layers. The sandy gravel layers correspond to the aquifer (i.e., layers two and four, see Table 1) are associated with a higher electrical resistivity (> 90 Ωm) due to a lower surface charge leading to a reduced surface conductivity. The impermeable layers with high clay content (i.e., layers one, three and five, see Table 1) are associated to a low electrical resistivity (< 30 Ωm), due to the contribution of both electrolytic and surface conductivity (e.g., Flores Orozco et al., 2011). In case of fine grains like clays, the large surface area and high surface charge enhances the accumulation of charges at the electrical double layer increasing the electric conductivity (e.g., Revil and Glover, 1998; Glover, 2015). Thus, the presence of fine grains reduces the resistivity and the effective porosity and subsequently also the hydraulic conductivity (e.g., Weller et al., 2015; Osterman et al., 2019). We investigate, in particular, how the sensitivity of the TEM method changes in relation to the intercalation of conductive and resistive media.

For the inversion of numerical data we forward model the data using the resistivity distributions described in Table 1, contaminate the data with 2.5% random noise and use the same TEM-FAST system settings as in the field experiment. To evaluate our inversion approach in the numerical example, we use an eight layer homogeneous initial model with a resistivity of 18 Ωm and a logarithmically increasing layer thickness to a cumulative depth of 120 m for both loop sizes. Field measurements where done in Burgenland, Austria (47°46′12.2″N 16°52′12.3″E) within the soda lakes of the "Nationalpark Neusiedlersee - Seewinkel" (Fig. 1b). This site offers a noise-free environment for testing our algorithms, as there is no infrastructure in the vicinity. Stratigraphic data (Fig. 1c) available from a historic borehole ca. 500 m to the south-west of the TEM sounding position revealed an 1.6 m thick clayey silt layer that is covering a sandy gravel aquifer. At a depth of 7.5 m there is another clayey silt layer which confines the aquifer and extends to the maximum drilled depth of 10.0 m m. The TEM measurements were conducted during May of 2022 in dry surface conditions. We used 4 A of transmitter current with both a 12.5 m loop and a 50.0 m loop for shallow and deep investigations, respectively. In the case of the 12.5 m loop, we obtained the voltage readings in 28 windows ranging from 4 μs to 512 μs by stacking the impulse response 8320 times, whereas we used 40 windows ranging up to 4096 μs and 4160 stacks for the 50.0 m loop. For the inversion, we filtered the data from 12.5 m to a time range of 5 μs to 200 μs and the data from 50.0 m loop to a time range of 12 μs to 4100 μs while using a ten layer homogeneous initial model with a resistivity of 18 Ωm and a logarithmically increasing layer thickness to a cumulative depth of 120 m for both loop sizes.

The numerical model associated to the second site corresponds to conductive and polarizable anomalies related to a graphite deposit within a resistive, non-polarizing host rock. Graphite is an electrical

conductor, therefore, it has a higher electrical conductivity and polarization (e.g., Revil et al., 2017, and Bücker et al., 2018) than the surrounding host rock. We investigate, in particular, changes in sensitivity of the TEM method due to the highly conductive and polarizable graphite layer on top of a resistive host rock. For the inversion of numerical data we forward the data using the model parameters described in Table 2, contaminate the data with 3.0% random noise and use the same TEM-FAST system settings as in the field experiment. To evaluate our inversion approach in the numerical example, we use the initial model described in Table 3. Field measurements were conducted in September of 2022 in dry surface conditions at the grounds of a former graphite quarry in Lower Austria, Austria (48°14′09.4″N 15°27′16.2″E, Fig. 1d). The investigated graphite deposit is embedded in a host rock that consists mainly of marble as shown by the geological map (Schnabel et al., 2012) in Fig. 1d. We used 4 A of transmitter current with a 12.5 m loop and we collected voltage readings in 28 windows ranging from 4 μs to 512 μs with 8320 stacks. For the inversion, we filtered the data from 12.5 m to a time range of 5 μs to 200 μs while using a five layer homogeneous initial model with a resistivity of 18 Ωm and a thickness of 5 m in the first layer and a thickness of 6 m in the last four layers. In the field data inversion we use a six layer initial model with equal layer thicknesses and constant resistivity of 18 Ωm. All layers except the first one exhibit IP effects with the same MPA model parameters as shown in the second layer of Table 3. We obtained complimentary data using the complex resistivity (CR) method with the DAS-1 system, manufactured by MPT-IRIS technologies deploying 32 stainless-steel electrodes separated by 3 m. Inversion results were obtained using the complex resistivity inversion algorithm CRTomo (Kemna, 2000) and the data error was quantified following the methodology described by Flores Orozco et al. (2012).

The third site corresponds to a highly resistive and polarizing layer, due to the presence of ice, which is a material with high electrical resistivity and high polarization at high frequencies (>1 kHz) (e.g., Mudler et al., 2019). We model the ice glacier below a 10 m thick snow cover and an ice thickness of 20 m which covers a resistive bedrock with negligible polarization (see Table 2). We investigate, in particular, the changes in sensitivity of the TEM method due to the the highly resistive and polarizable ice layer on top of a less resistive and non-polarizing bedrock. For the inversion of numerical data we forward model the data using the model parameters described in Table 2, contaminate the data with 3.0% random noise and use the same TEM-FAST system settings as in the field experiment. To evaluate our inversion approach in the numerical example, we use the initial model described in Table 3. Field data were collected in June of 2021 at the "Kleinfleißkees" glacier (47°03′11.8″N 12°57′23.8″E) with a varying ice thickness that shows a maximum of 20 m on top of a compact gneiss bedrock. The study site is located below the peak of the Hoher Sonnblick, Salzburg, Austria and Fig. 1e depicts the extent of the glacier which was covered by ca. 6 m of wet snow during TEM measurements. We used 4 A of transmitter current with a 50.0 m loop and we collected voltage readings in 28 windows ranging from 4 μs to 512 μs with 33,280 stacks. For the inversion, we filtered the data to a time range of 12 μs to 100 μs while using a five layer initial model with a thickness of 3 m in the first four layers and a thickness of 6 m in the fifth layer. All layers except the first and last one exhibit IP effects with the same MPA model parameters as shown in the second layer of Table 3. We also provide a resistivity contrast of 300 Ωm to 3000 Ωm between the non-polarizing and polarizing layers, respectively.

4. Results

4.1. Case study 1: conductive layered media without IP effects

Fig. 2 shows the forward response (Fig. 2a) and inversion results (Fig. 2b) of a 12.5 m loop for a five layer model with varying resistivity that represents two aquifers (second and fourth layers) separated by two

Table 1

Overview of the model parameters for numerical data at the soda lakes site including the layer thickness thk and the electrical resistivity ρ. This resistivity distribution represents two aquifers separated by impermeable layers with high clay content.

Layer	thk(m)	ρ (Ω m)	Material
1	4	25	clay-rich top layer
2	10	100	first aquifer
3	20	15	clay-rich confining layer
4	20	150	second aquifer
5	∞	15	clay-rich confining layer

Table 2

Overview of the model parameters for numerical data at the graphite deposit site and the ice glacier site including the layer thickness thk and the electrical resistivity ρ (different for the two sites), as well as the maximum phase angle model parameters, namely (same for the two sites): the maximum phase angle ϕ_{max}, the relaxation time τ_ϕ and the dispersion coefficient c.

Layer	Graphite deposit			Ice-glacier site			ϕ_{max} (rad)	τ_ϕ (s)	c ()
	thk (m)	ρ_0 (Ω m)	Material	thk (m)	ρ_0 (Ω m)	Material			
1	8	50	soil layer	10	500	wet snow cover	0.0	1e-6	0.1
2	12	10	graphite deposit	20	3000	ice glacier	0.8	5e-2, 5e-4	0.9
3	∞	500	host rock	∞	300	bedrock	0.0	1e-6	0.1

Table 3

Overview of the initial model parameters for numerical data at the graphite deposit site and the ice glacier site including the layer thickness thk and the electrical resistivity ρ (different for the two sites), as well as the maximum phase angle model parameters, namely (same for the two sites): the maximum phase angle ϕ_{max}, the relaxation time τ_ϕ and the dispersion coefficient c.

Layer	Graphite deposit		Ice-glacier site		ϕ_{max} (rad)	τ_ϕ (s)	c ()
	thk (m)	ρ_0 (Ωm)	thk (m)	ρ_0 (Ωm)			
1	10	50	11	400	0.0	1e-6	0.1
2	10	50	14	6000	0.6	1e-2, 1e-4	0.6
3		50		400	0.0	1e-6	0.1

aquitards corresponding to clay rich materials (third and fifth layers, see Table 1). In a first step, we will evaluate our inversion scheme by comparing the inverted and the true model. The inversion yields an accurate data fit ($\chi^2 = 0.8$, rRMS = 2.8%) and we observe that the resistivity and thickness of the conductive (i.e., clay-rich, < 50 Ωm) first, third and fifth layers is better resolved than the resistivity and thickness of the aquifers (related to the high resistive second and fourth layers).

The resistivity of the second and fourth layers are slightly underestimated compared to the true model values. The thickness of the second layer of the true model is well resolved, but the thickness of the third layer is overestimated by the inverted model. Fig. 2c and Fig. 2d show the forward response and inversion results of a 50.0 m loop and the inversion yields an accurate data fit ($\chi^2 = 0.7$, rRMS = 2.7%), yet the inverted models show also a deviation from the true model values in particular for the resistive second and fourth layers. Similar to the inversion result of the 12.5 m numerical data inversion, the aquitard (related to the conductive layers) of the inverted model obtained from numerical data with a 50.0 m are much closer to their corresponding true model values.

The depth of investigation (DOI) of the 50.0 m loop (147 m) is almost twice as deep as the DOI of the 12.5 m loop (81 m), which indicates the superior sensitivity at depth of the 50.0 m loop. The DGSA results in Fig. 2e to Fig. 2h reveal that the two geometries are well suited for our investigated numerical experiments, with the data being sensitive to most of the parameters resolved by the inversion. The first layer is the most influential parameter for both loop sizes, as expected as it is associated to a higher signal-to-noise ratio. Fig. 2d and Fig. 2h show that the resistivity of the second to the fourth layer are influential for both loop sizes, yet the 50.0 m loop data is also sensitive to the resistivity of
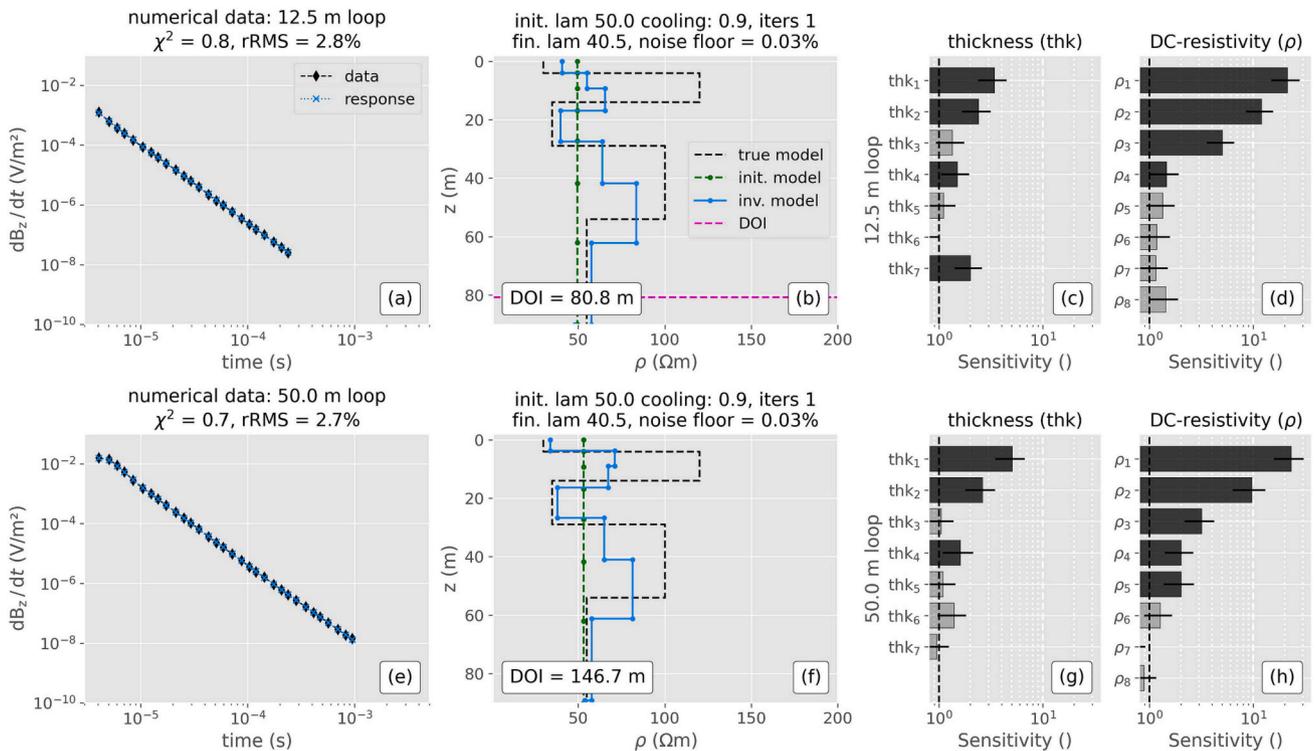
Fig. 2. Inversion results in terms of the data fit and retrieved models from numerical data (a, b, e and f) for a 12.5 m loop (a and b) and a 50.0 m loop (e and f). Panels (c), (d), (g) and (h) show model parameter sensitivity from the distance-based generalized sensitivity analysis (DGSA) using 20,480 model responses. The vertical dashed line indicates the threshold of 1 (i.e., larger sensitivities indicate influential parameters) and the horizontal black lines the confidence interval of the corresponding sensitivity.

the fifth layer. Additionally, Fig. 2c and Fig. 2g reveal that the data from both loops are sensitive to the layer thickness of the first, second and fourth layer, which corresponds well to the high sensitivity obtained from DGSA. The high sensitivity of the conductive (i.e., clay-rich) first and fourth inverted layer correspond well to the inversion results which show the best true model recovery for the conductive first and fourth layer. The DOI predicts in general that the TEM method is sensitive at depths where our DGSA results reveal a poor sensitivity for both the layer thickness as well as the layer resistivity indicating that the DOI might overestimate the sensitivity of the numerical TEM data at depth in our experiment.

Fig. 3 shows inversion results of field data for the 12.5 m (Fig. 3a and Fig. 3b) and 50.0 m loops (Fig. 3e and Fig. 3f) measured at the soda lake. We interpret the inverted models from both loops as a four layer model consisting of a shallow (3 m to 12 m) and a deep (at depths below ca. 35 m) aquifer. The shallow aquifer is characterized by a lower electrical resistivity ca. 20 Ωm than the deep aquifer (ca. 30 Ωm) indicating a higher clay content in the shallow aquifer. The depth to the shallow aquifer is in agreement with the lithological change observed in the borehole data (see Fig. 1b), but the thickness of the aquifer is ca. 5 m larger in the TEM inversion model which is likely related to the offset between the TEM sounding position and the borehole. The aquifers are separated by an aquiclude (i.e., layer with high clay content) characterized by an electrical resistivity below ca. 15 Ωm ranging from 12 m to 35 m. Furthermore, the first conductive layer (up to 3 m depth) is only solved by inversion of the 12.5 m loop data, whereas the 50.0 m loop solves for lower resistivity (30 Ωm) in the bottom aquifer.

The DGSA results (Fig. 3c,d and Fig. 3g, h) reveal that the data is more sensitive to the resistivity of the layers than to the thickness of the layers. As expected considering the higher signal-to-noise ratio, more layers of the result from the 50.0 m loop are influential on the model response than for the 12.5 m loop. This increased sensitivity is in accordance with the larger DOI of the 50.0 m loop, yet our DGSA results

show that the DOI overestimates the maximum depth where we have reliable data when compared to the DGSA, likely evidencing the improved ability of the DGSA to evaluate the maximum depth reached with the TEM method. Furthermore, our DGSA results reveal that the TEM method in a single-loop configuration can resolve the distribution of the electrical resistivity and the geometry of two aquifers.

4.2. Case study 2: conductive layered media with IP effects

Fig. 4 shows the forward responses of a 12.5 m loop comparing three different cases (see Table 2): (a) corresponds to non-polarizing media. (b) has a polarizable second layer with a relaxation time τ_ϕ of 50 ms, whereas (c) has a polarizable second layer with a τ_ϕ of 0.5 ms. Fig. 4a shows a smooth decay for the observed secondary magnetic field over 6 orders of magnitude (10^{-3} V/m^2 to 10^{-9} V/m^2), with a change of slope in a time range from 10 µs to 100 µs due to the conductive layer in the resistive host media. The rate of decay increases slightly at approximately 100 µs which hints at the high resistivity of the bottom layer. The overall signal shape in Fig. 4b is similar to case (a), but the decay curve stretches over only 4 orders of magnitude (10^{-3} V/m^2 to 10^{-7} V/m^2) and is shifted to higher values in the secondary magnetic field. Although the second layer is polarizable, we can not observe negative voltage readings in case (a) associated to a τ_ϕ of 50 ms. This case is especially critical, as such curves are affected by IP effects, but may be overlooked due to the absence of negative voltage readings; hence we will refer to this case as the positive IP effect ($\oplus$IP). Usage of a resistivity-only inversion will lead to erroneous resistivity models as demonstrated by Viezzoli and Manca (2020) and Grombacher et al. (2021). Fig. 4c shows that IP effects associated to a low τ_ϕ of 0.5 ms results in sign-reversals (i. e., negative voltage readings) after 220 µs and all remaining 9 voltage readings stretch over 4 orders of magnitude (10^{-3} V/m^2 to 10^{-7} V/m^2). We will, therefore, refer to this case as the negative IP effect ($\ominus$ IP) and such case evidences the contamination of TEM data due to IP effects
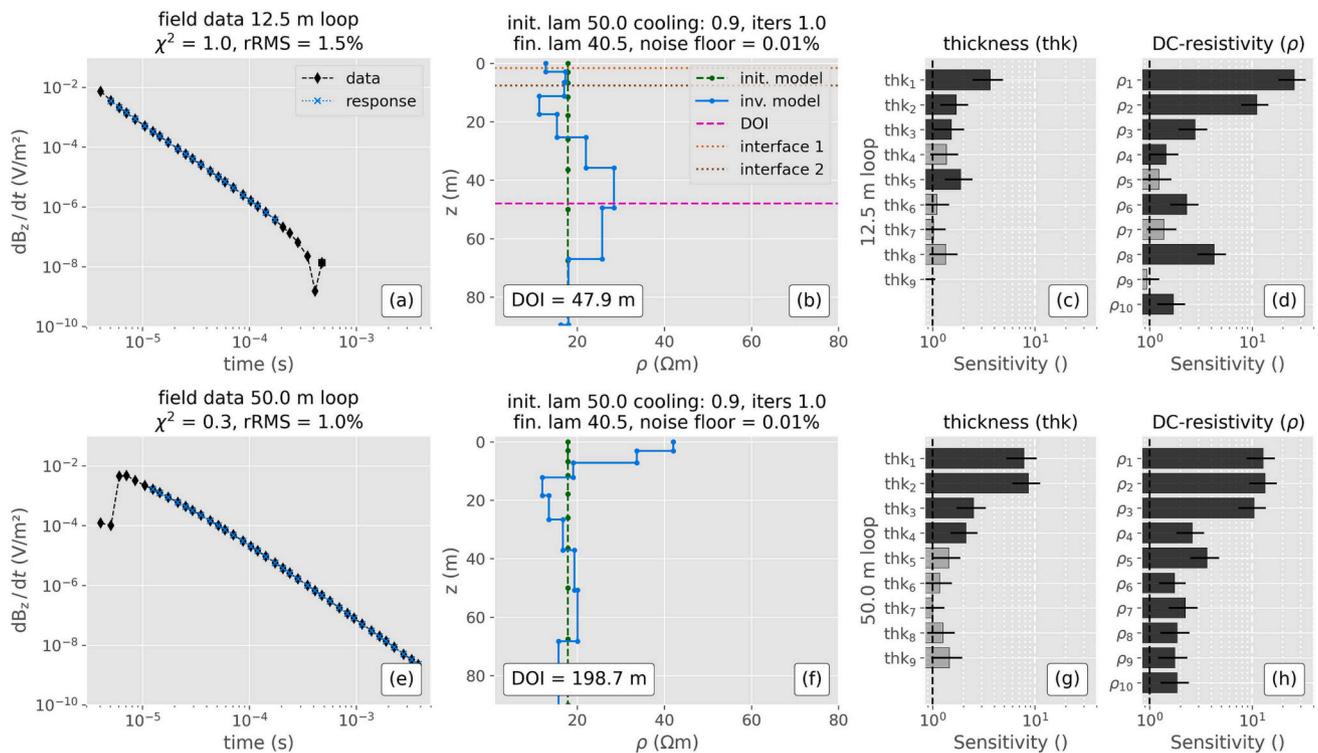
Fig. 3. Inversion results in terms of the data fit and retrieved models from field data (a, b, e and f) for a 12.5 m loop (a and b) and a 50.0 m loop (e and f). The interfaces one and two are related to the contact between clays to sandy gravels (top confining layer), and to the contact between sandy gravels to clays (bottom aquitard), respectively (see Fig. 1b). Panels (c), (d), (g) and (h) show model parameter sensitivity from the distance-based generalized sensitivity analysis (DGSA) using 20,480 model responses generated for the corresponding inverted models.
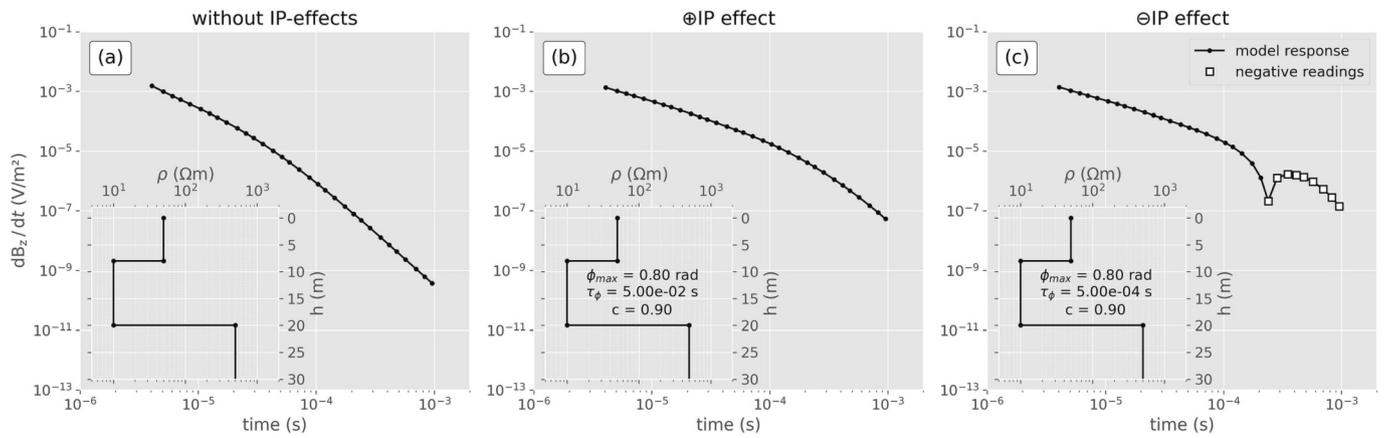
Fig. 4. Three TEM forward responses of a conductive three layer model with a graphite-rich second layer. The sub panels in the lower left corner of all subplots shows the electrical model of the subsurface. (a) is the reference case without any IP effects. (b) is affected by the IP effect in layer two with a relaxation time (τ_ϕ) of 50 ms. (c) is also affected by the IP effect but with a τ_ϕ of 0.5 ms.

where the negative voltage readings are not related to noise. A detailed analysis of the polarization mechanism causing negative voltage readings can be found in Kang et al. (2020).

Fig. 5 presents the inversion results of numerical data for the ⊕IP case and the ⊖ IP case. We model the IP effect only in the second layer and fix ϕ_{max} of the first and third layer to 0.0 rad. Fig. 5b and Fig. 5h show the sensitivity of all model parameters and we observe that the thickness of the first layer (i.e., the depth to the polarizable layer) is influential on the model response in both cases which is in agreement with the correct parameter retrieval by the numerical data inversion. The inversion results hint also at a correct retrieval of the thickness of the second layer for both the ⊕IP case and the ⊖ IP case, however, the DGSA reveals that the thickness of the second layer is non-influential in the ⊕IP case and inconclusive (i.e., sensitivity minus confidence interval not greater 1) in the ⊖ IP case. Such discrepancies might point to the importance of selecting an adequate initial model to run the inversion, which will be discussed in the next chapter. The ⊕IP effect case is sensitive to the resistivity of all three layers, however the numerical inversion results fail to retrieve the true model value of the third layer, indicating the increased non-uniqueness of the ⊕IP effect case.

The target of the geophysical survey is the depth to and the thickness of the polarizable layer; hence, the DGSA provides valuable information to which extent we can rely on the resolved values of those two parameters. The ϕ_{max} and c parameters are influential on the model response for both cases while it is statistically inconclusive whether or not τ_ϕ is influential on the response for both cases. The high sensitivity of ϕ_{max} and c in the both cases agrees well with the inversion result that is close to the corresponding true model value.

Fig. 6 shows the imaging of the inversion results of field data obtained along a single profile at the investigated former graphite quarry. All soundings converge to an rRMSE below 6% and we are able to model all soundings with an ⊕IP effect, as there are no negative voltage readings in the data (see Appendix A.4). We consistently solve for a three layer model with lateral variations in the parameters ρ_0 and ϕ_{max}, whereas c shows only slight variations. The first layer shows the largest lateral variations in ρ_0 with two high resistive anomalies ($> 60~\Omega m$) between 0 m and 25 m as well as between 50 m and 100 m profile distance. The second layer is characterized by significantly lower ρ_0 values ($< 30~\Omega m$) and the lowest values ($< 15~\Omega m$) are observed between 40 m and 160 m profiles distance. Furthermore, ϕ_{max} shows a slight increase from 0.1 rad to 0.4 rad in depths below 5 m, yet we observe lower values of ϕ_{max} between 50 m and 100 m profile distance, which is co-located with a resistive anomaly. The ϕ_{max} values in layer two are higher (> 0.5 rad) between 75 m and 160 m profile distance as well as at the last (L13) of the profile than in the remaining areas of the

section. The bottom layer shows mainly intermediate ρ_0 values (ca. 30 Ωm) with an anomaly between 0 m and 25 m profile distance that is slightly less resistive. We interpret conductive anomalies that show a resistivity below 15 Ωm and ϕ_{max} above 0.6 rad as the graphite rich areas in the subsurface. The relaxation time τ_ϕ shows no lateral or vertical variations at a τ_ϕ of ca. 1×10^{-4} seconds and thus is not shown here.

So far we have evaluated our inversion routines for TEM data including IP effects only by means of numerical experiments. However, field data are more challenging due to the numerous sources of error and changes in signal strength, which cannot be reproduced in numerical experiments. The TEM profile collected at the graphite deposit provides an excellent opportunity to compare the TEM inversion with results obtained through the application of complex-resistivity (CR) electrical measurements at 1 Hz. Fig. 6d shows similar lateral changes in the solved electrical resistivity as both methods solve for a three layer model with a highly conductive anomaly in the second layer between 40 m and 180 m.

The TEM results show electrical resistivities in a lower range than the CR results (15 Ωm to 100 Ωm in TEM and 25 Ωm to 500 Ωm in CR), which is likely related to the different measurement volumes of the two methods. Yet, the conductive anomaly between 125 m and 180 m CR profile distance is consistently resolved in both methods and related to the graphite rich layer. Additionally, the TEM inversion results show a sharp contrast at the interface between the second and third layer (ca. 30 m depth), which is not as clearly resolved by the CR method. Lateral changes close to the surface (ca. 5 m) are better resolved in the CR results likely due to the large spacing between TEM soundings leading to averaged resistivity values in the first 5 m to 10 m. The quantitative comparison between ϕ_{max} (from the TEM method) and the inverted phase angle ϕ (from the IP method) in Fig. 6e might be limited as the two subsurface properties where obtained at two entirely different measurement frequencies (kHz range for the TEM method, at 1 Hz for the CR method). However, we observe a similar increase of the values (up to 0.7 rad for ϕ_{max} and up to 100 mrad in ϕ) starting at 115 m profile distance, while the TEM method solves for a sharp contrast in ϕ_{max} at a depth of 30 m.

Fig. 7 shows the sensitivities of the model parameters for the inversion results of field data measured at at the graphite deposit. We selected sounding positions L03 and L12 (Fig. 6, at 50 m and 160 m profile distance), as they represent two different subsurface models along the investigated profile. The sensitivities of the L03 and L12 models show that the thickness and resistivity of the first two layers are the most influential parameters. We observe a decrease of the sensitivity with depth for all model parameters at L03 (Fig. 7a to Fig. 7e). Yet, the TEM
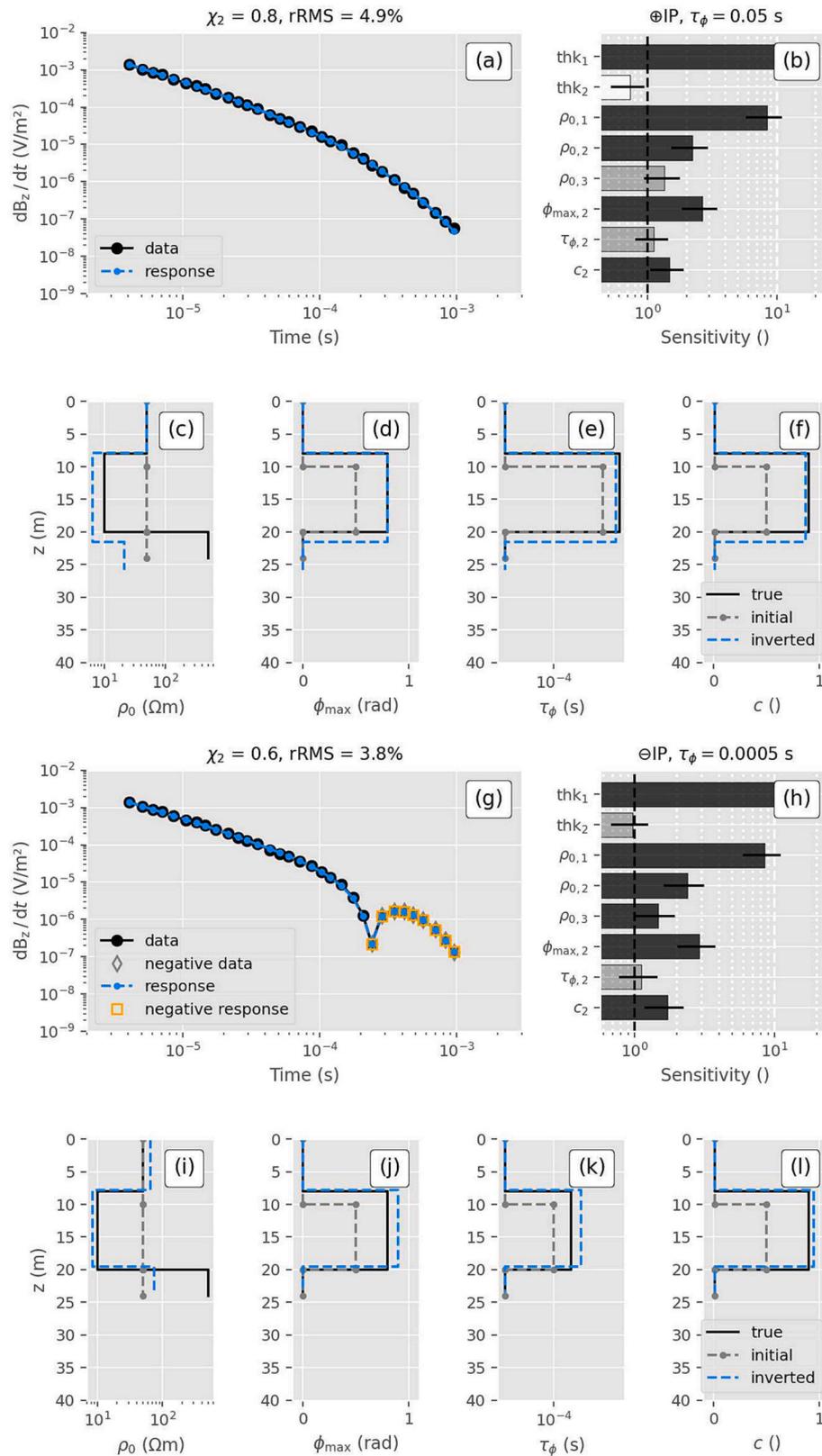
Fig. 5. Data fit - (a) and (g) - and inversion results - (c) to (f) and (i) to (l) - using numerical data from the graphite deposit example. Panels (b) and (h) show the corresponding DGSA results. Panels (c) and (i) show the electrical resistivity, (d) and (j) the maximum phase angle ($\phi_{\max}$), (e) and (j) the relaxation time (τ_ϕ) and (f) and (l) the dispersion coefficient c. The two top rows (a) to (f) correspond to the case with a relaxation time (τ_ϕ) of 50 ms, resulting in the positive IP effect ($\oplus$IP). The two bottom rows (g) to (l) correspond to the example with a relaxation time (τ_ϕ) of 0.5 ms, resulting in the negative IP effect ($\ominus$ IP).
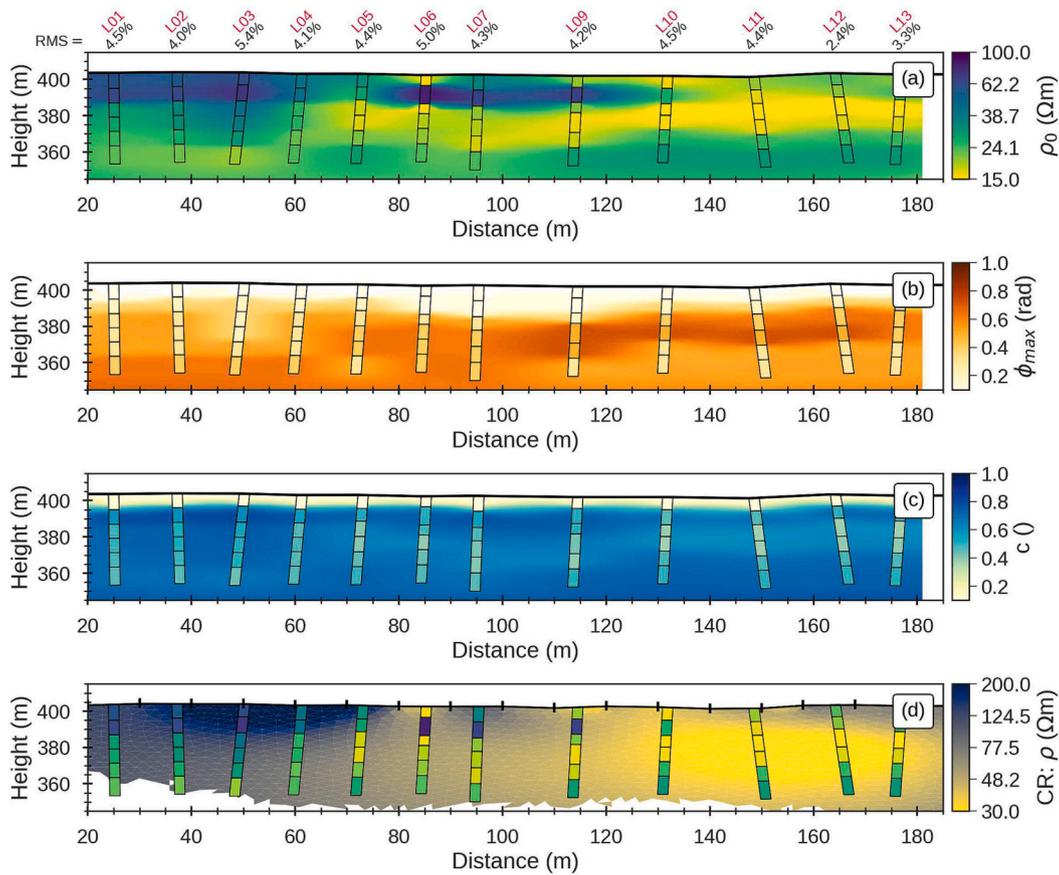
Fig. 6. 2D section of the maximum phase angle model parameters obtained from inversion of field data collected at a graphite deposit. The black rectangles indicate the 1D inversion models at the individual sounding positions, whereas the background colors are obtained through interpolation. (a) shows the DC resistivity ρ_0 in Ω m, (b) the maximum phase angle ϕ_{max} in rad, (c) the dispersion coefficient c and (d) a comparison of the 1D TEM inversion models from (a) to SIP data measured along the same profile (the colormap of the TEM results is show in panel a).
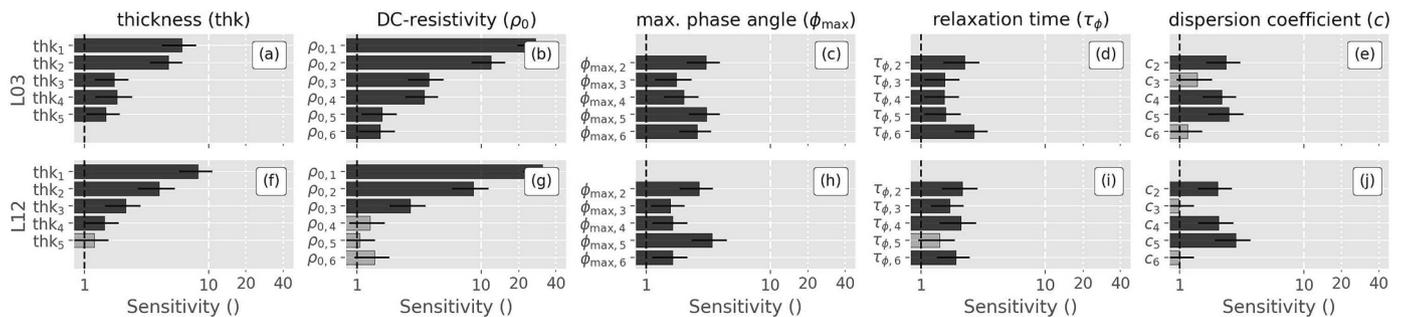
Fig. 7. Distance-based generalized sensitivity analysis (DGSA) of the inverted field data results at sounding positions L03 (a to e) and L12 (f to i) along the graphite deposit profile. The vertical dashed line indicates the threshold of 1 (i.e., larger sensitivities indicate influential parameters) and the horizontal black lines the confidence interval of the corresponding sensitivity.

data measured at L03 is more sensitive to the thickness of the fourth and fifth layer (Fig. 7f) as well as to the resistivity of the fourth, fifth and sixth layer (Fig. 7g) than at L12. This decreased sensitivity at L12 is likely related to the higher resistivity which results in a larger uncertainty of the actual resistivity values solved below the graphite layer. Furthermore, similar to the numerical example, we also observe here that τ_ϕ and c are less influential than ϕ_{max}. Our sensitivity results show the capability of the TEM method to determine the depth to and the resistivity of the bottom layer along the investigated profile, as well as to obtain reliable values of ϕ_{max}. This highlights the improved sensitivity at depth of the selected 12.5 m single-loop configuration compared to the deployed measurement configuration and survey layout of the CR

method.

The collection of TEM data in conductive environments is clearly favorable for the TEM method as we observe high sensitivities in most model parameters. We believe that the use of the DGSA, as presented in Fig. 7, provides critical information to evaluate the reliability of the electrical model obtained in the inversion and can help to provide a better interpretation. Additionally, the DGSA might improve the quantification of graphite content from TEM measurements, although this issue is beyond the scope of this study.

4.3. Case study 3: resistive layered media with IP effects

Fig. 8 shows the forward responses of a 50.0 m loop numerically simulating an ice glacier represented by a three layer model, where the second layer corresponds to a high resistivity (5000 Ωm) associated to a pure ice layer. Similar to the graphite case study, we forward model three different scenarios (see Table 3): (a) corresponds to non-polarizing media. (b) has a polarizable second layer with a relaxation time τ_ϕ of 50 ms, whereas in (c) the polarizable second layer has a τ_ϕ of 0.5 ms. Besides the turn-off ramp effect affecting the first three voltage readings, Fig. 8a shows a smooth decay of the observed secondary magnetic field over 10 orders of magnitude in absence of IP effects, with a change of slope at ca. 8 μs related to the turn-off ramp of the current pulse while the remaining decay curve (after 10 μs) shows no deviations from a straight line. Although, the decay curve in Fig. 8b is affected by the $\oplus$IP effect in the second layer, we observe the same shape as in Fig. 8a, which demonstrates that a τ_ϕ of 50 ms leads to the polarization affecting the TEM response above the acquisition time. A lower τ_ϕ of 0.5 ms leads to the $\ominus$ IP effect and the decay curve has a sign-reversal at 100 μs that affects all following 15 voltage readings indicating the presence of IP effects. As the $\oplus$IP case and the non-polarizable case are similar and haven discussed to a certain extent in the previous case study, the upcoming numerical data inversions of the ice glacier are only calculated for the model parameters of case (c).

Fig. 9 shows the inversion results using the numerical data from Fig. 8c representing the $\ominus$ IP case. We model the IP effect only in the second layer and fix $\phi_{\max}$ of the first and third layer to 0.0 rad. Fig. 9a shows an accurate data fit ($\chi^2 = 1.8$, rRMSE = 8.4%) and the negative voltage readings are modelled with the correct sign and magnitude. The sensitivities of the TEM model parameters (see Fig. 9b) reveal that the most influential parameters are the resistivity of the first and second layer as well as $\phi_{\max}$ of the second layer. The high sensitivity for the resistivity of the first layer corresponds to a low difference between the true and inverted model values (see Fig. 9b), whereas the resistivity of the second layer shows a larger difference between the true and inverted model values. Furthermore, we observe a small difference between the true and inverted model values of $\phi_{\max}$ (see Fig. 9d). The resistivity of the third layer is significantly less influential as they are statistically inconclusive (i.e., sensitivity minus confidence interval not greater 1), yet the inversion recovers the true model value, which might be only related to the choice of the initial model. Furthermore, the thickness of the first and second layer, as well as τ_ϕ of the second layer are statistically inconclusive on the model response, yet the inversion recovers the true model values accurately which is likely also related to the initial model values. Despite c having a sensitivity being below 1, the inversion

recovers the true model values. Clearly, the use of the TEM method in highly resistive environments pushes the method to its limit; thus the DGSA provides valuable information to assess the reliability of the inverted model parameters.

Fig. 10 shows the imaging plane obtained from the inversion results of field data along the investigated ice glacier. We use a six layer initial model, where all layers except the first and last one include IP effects, i. e., $\phi_{\max}$ was fixed to 0.0 rad). The soundings converge to an rRMSE between 15% and 26% and we are able to model all soundings with an $\ominus$ IP effect, as there are negative voltage readings in the data (see Appendix A.4). We obtain a three layer model with no significant lateral variations in all parameters observing a $\ominus$ IP effect after ca. 40 μs. The first layer is ca. 5 m thick and shows an electrical resistivity of ca. 300 Ωm without IP effects corresponding to the wet snow cover of the ice glacier. The second layer has a thickness varying between 10 m to 13 m, an electrical resistivity up to 5000 Ωm and a $\phi_{\max}$ larger than 0.6 rad, corresponding to the ice unit. This corresponds well to preceding TEM studies that also observed strong IP effects in frozen media (e.g., Kozhevnikov and Antonov, 2012; Grombacher et al., 2021). The bottom layer is located at a depth of approximately 20 m and shows an electrical resistivity of 300 Ωm, corresponding to the underlying gneiss bedrock. The low electrical resistivity values point to a fractured bedrock filled with sediments. The relaxation time τ_ϕ shows no lateral or vertical variations at a τ_ϕ of ca. 5×10^{-5} seconds and thus is not shown here.

Fig. 11 shows the model parameter sensitivities at sounding position L50–8 (see Fig. 10). The other soundings reveal consistent results and are not shown here to avoid redundancies. The model parameters for all layers of $\phi_{\max}$ and the layer thicknesses are influential on the model response, which evidences that the TEM method is able to estimate the thickness of the snow cover and the depth to the bedrock. Furthermore, ρ_0 of the first and sixth layer more influential on the model response than ρ_0 of the second to fourth layers, which is likely related to the high resistivity of the ice-rich layers. The response is less sensitive to τ_ϕ and c, because all parameters show overall lower sensitivity with τ_ϕ of the third and fifth layer as well as c of the third layer showing a sensitivity that is statistically inconclusive.

The collection of TEM data in high resistive environments is clearly limited by low signal strength, hindering deep investigations, at least with the TEM-FAST system deployed here. On one hand, the use of instruments with higher magnetic momentum are desired; on the other hand, those devices commonly require heavier components, which might limit the deployment in difficult terrain and remote areas. Hence, the use of the TEM-FAST system may represent the only possibility for an initial investigation with the TEM method. State-of-the-art ice glacier investigations rely on ground penetrating radar (GPR) measurements,
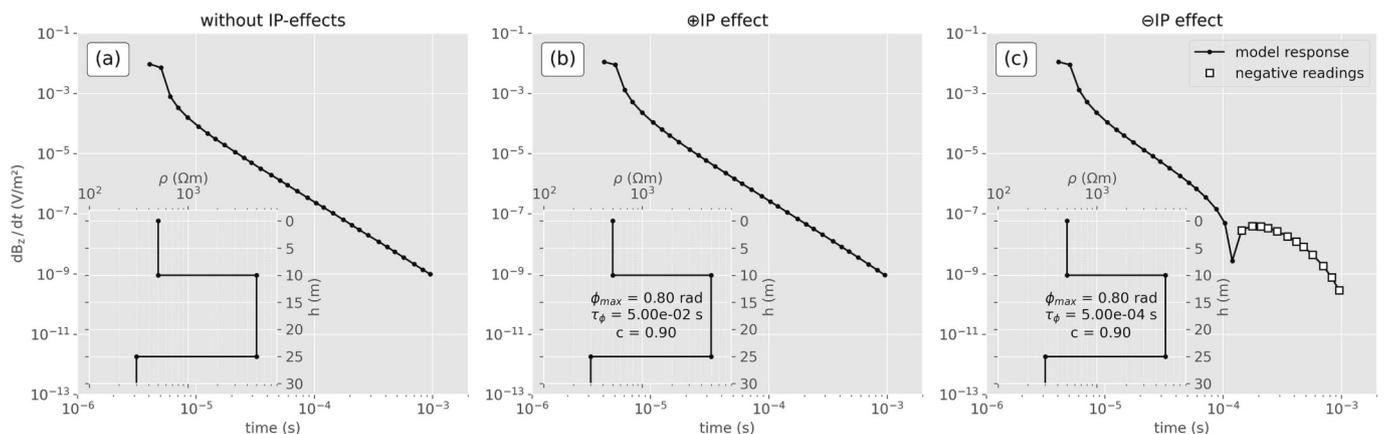
Fig. 8. Three TEM forward responses of a three layer resistive model, which simulates an ice glacier. The sub panels in the lower left corner of all subplots shows the electrical model of the subsurface. (a) is the reference case without any IP effect. (b) is affected by the IP effect in layer two with a relaxation time (τ_ϕ) of 50 ms. (c) is also affected by the IP effect in layer two but with a smaller τ_ϕ of 0.5 ms.
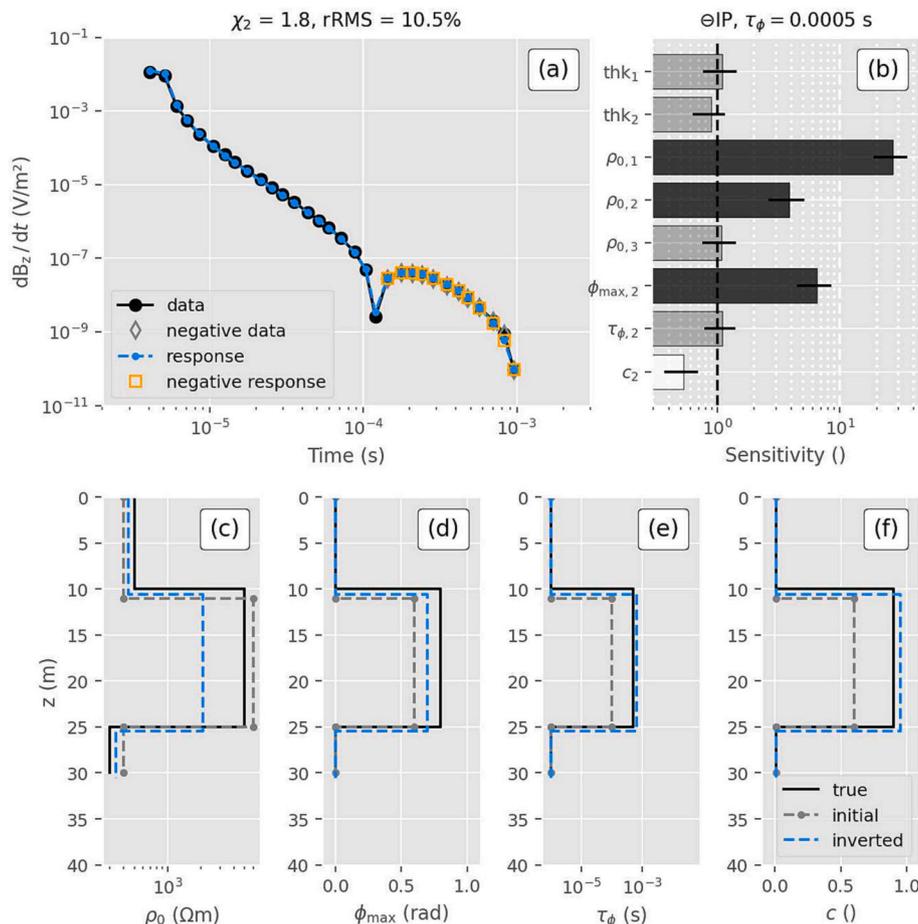
Fig. 9. Data fit (a) and inversion results (c) to (f) using numerical data from the ice glacier example. Panel (b) shows the model parameter sensitivity obtained from the DGSA. Panel (c) shows the electrical resistivity, (d) the maximum phase angle (ϕ_{max}), (e) the relaxation time (τ_ϕ) and (f) the dispersion coefficient c.

but GPR may not permit to evaluate the properties of the bedrock. Or DGSA results demonstrate that the TEM method is well suited to resolve the resistivity of the bedrock and the thickness of the ice glacier; thus, making the TEM method in a single-loop configuration a potential tool for investigations of alpine permafrost, especially in confined areas with poor access and difficult terrain.

Results presented in Fig. 10 demonstrate that even with the 4 A transmitter current of the TEM-FAST system, the data can provide some useful results and delineate the geometry of ice-rich areas, as required for permafrost investigations (e.g., Mudler et al., 2019; Maierhofer et al., 2022). We believe that the use of the DGSA, as presented in Fig. 11, provides relevant information to evaluate the reliability of the retrieved electrical models. In this regard, we can rely on our estimation of the thickness of the snow cover as well as the thickness of the layer corresponding to the ice glacier. Future investigations should consider the inclusion of structural constraints such as prior information on snow and ice thickness from complimentary geophysical data like GPR. Such prior information should help to reduce the non-uniqueness in the inversion and obtain an improved inversion result (e.g., Aigner et al., 2021 for waterborne TEM measurements). Moreover, future work should also investigate a likely increase of DGSA sensitivity obtained through the inclusion of constraints.

5. Discussion

Our results demonstrate the applicability of our forward modeler to generate the single-loop response of the TEM-FAST system by modeling the system parameters (see Appendix A.1). We validate our forward model by comparing it to existing commercial and open-source algorithms (see Appendix A.2). Furthermore, we include include the frequency-dependence of the complex resistivity by applying the maximum phase angle model proposed by Madsen et al. (2017). We show that such forward modeler can be used to develop open-source deterministic inversion routines as well as for the analysis of TEM data in stochastic frameworks such as the DGSA, which is applied to compute the sensitivity of the inverted model parameters. We only demonstrate the applicability of our inversion routines for blocky inversion approaches, but other inversion approaches can be investigated with our routines. Moreover, we have demonstrated through numerical experiments that our inversion approach is suited to handle TEM measurements including IP effects.

The DOI is a well-established method to assess the maximum depth at which TEM inversion results are reliable. Commonly, the DOI is calculated either from the skin-depth approach (e.g., Yogeshwar et al., 2020; Bücker et al., 2021), which is based upon the seminal work of Spies (1989), or from evaluation of the Jacobian matrix obtained after the final iteration of the inversion (e.g., Christiansen and Auken, 2012; Fiandaca et al., 2015; Grombacher et al., 2021; Maurya et al., 2022). However, such DOI approaches provide only a maximum depth to which the inversion result can be relied on, but do not offer any information on the influence of the model parameters above the DOI. Our DGSA results obtain the model parameter sensitivity in a statistical manner and reveal how the sensitivity of the thickness and electrical resistivity varies. In general, our DGSA results reveal that the electrical resistivity is more influential than the layer thickness for our numerical and field data examples. Despite the lower sensitivity of the layer thickness, the high
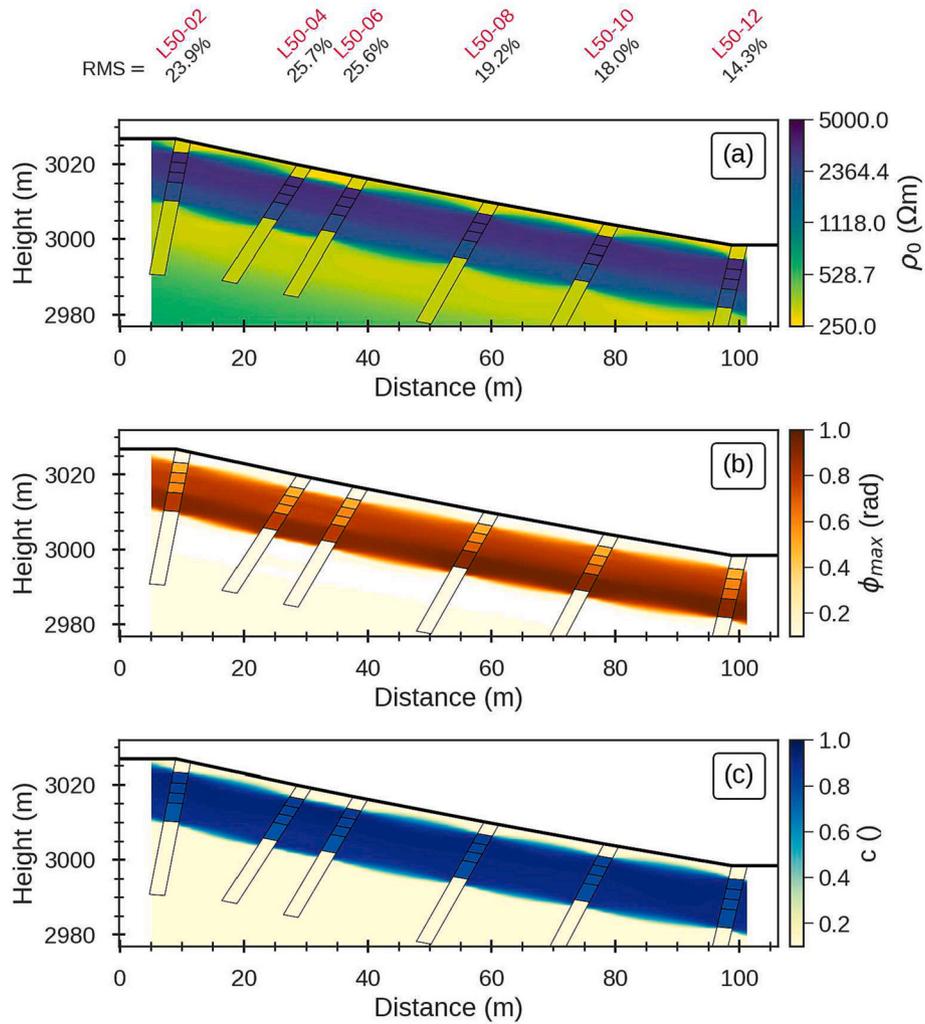
Fig. 10. 2D section of the maximum phase angle model parameters obtained from inversion of field data collected at an ice glacier. The black rectangles indicate the 1D inversion models at the individual sounding positions, whereas the background colors are obtained through interpolation. (a) shows the DC resistivity ρ_0, (b) the maximum phase angle ϕ_{max}, (c) the relaxation time τ_ϕ and (d) the dispersion coefficient c.
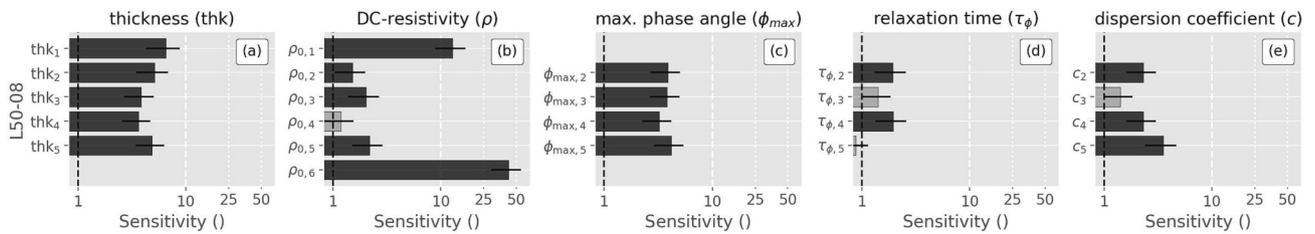
Fig. 11. Distance-based generalized sensitivity analysis (DGSA) of the inverted field data result at the ice glacier profile using the sounding position L08. The vertical dashed line indicates the threshold of 1 (i.e., larger sensitivities indicate influential parameters) and the horizontal black lines the confidence interval of the corresponding sensitivity.

sensitivity of the layer resistivity helps to distinguish between the two disconnected aquifers of our numerical experiment, because the DGSA results allow us to rely on the vertical variation of the electrical resistivity. Furthermore, we demonstrate that the DOI method based on the skin-depth approach overestimates the sensitivity of the TEM method for retrieving model parameters at greater depths in the case of conductive non-polarizable layered media.

In numerical experiments for conductive polarizable media, we observed the $\oplus$IP effect for a τ_ϕ of 50 ms and the $\ominus$ IP effect for a τ_ϕ of 0.5 ms. Such observation is similar to the work by Kang et al. (2020),

who report four different cases in numerical 3D modeling examples for airborne TEM data, yet their study investigates the effect of the depth to a chargeable cylinder and the conductivity contrast to the host rock in a numerical parameter study. Our numerical data experiments reveal that an adequate initial model is required to facilitate convergence of the inversion. In particular, our DGSA results show that parameters related to a low sensitivity (e.g., the layer thickness, τ_ϕ and c) have to be closer to the true model values than parameters which have a high sensitivity (e.g., ρ_0 and ϕ_{max}).

The sensitivity of TEM model parameters including IP effects ob-

tained from the DGSA at the graphite deposit case study demonstrate that we can rely on our estimation of the depth to and the thickness of the graphite rich layer. Additionally, our DGSA results show that the τ_ϕ and c are less influential on the model response than the other parameters. Nonetheless, our values for ϕ_{max}, τ_ϕ and c are in agreement with the values obtained by Maurya et al. (2022) from tTEM data. Furthermore, our τ_ϕ values retrieved from TEM field data are in a similar range (5×10^{-5} s to 5×10^{-4} s) when compared to spectral induced polarization (SIP) data collected in the laboratory on graphite samples (e.g., Abdulsamad et al. (2019), relaxation time from 10^{-2} s to 10^{-7} s) over a wide range of measurement frequencies (10^{-2} Hz to 10^5 Hz). At the field scale, the TEM method requires simplified field procedures compared to the SIP method, while also offering a larger DOI for confined survey layouts. Furthermore, the SIP method is limited at the field case in conductive environments by electromagnetic coupling effects already at 5 Hz (e.g., Flores Orozco et al., 2021), which complicates the correct estimation of small τ_ϕ values due to their linkage to high frequencies. Our TEM inversion routines demonstrate also that they are capable of resolving a sharper contrast between conductive anomalies, thus permitting a better delineation of graphite ores.

In numerical experiments for resistive polarizable media, the DGSA results reveal that resistive media reduce the sensitivity of our data to the inverted model parameters compared to the conductive media experiments. In particular, we observed that an adequate initial model is of higher importance to facilitate the convergence of the inversion than in the conductive media experiment. In particular, our results showed that parameters with a low sensitivity (e.g., the layer thickness τ_ϕ and c) have to be closer to the true model values than parameters with a high sensitivity (e.g., ρ_0 and ϕ_{max}). Such observation is in agreement with the studies by Lin et al. (2019) and Grombacher et al. (2021) who suggest to fix τ_ϕ and c in the first 10 iterations of the inversion as this helps to improve convergence. Similar to the conductive numerical experiment, resistive media require a clear contrast in the ϕ_{max}, τ_ϕ and c parameters, yet they also require a contrast in ρ_0 to facilitate the convergence of the inversion. Hence, for resistive media it is favorable to have prior information on the location of the polarizable layer within the subsurface.

Investigations in resistive media are at the limit to collect TEM data, at least with the instrument deployed here, as observed in our Fig. 10. Nonetheless, our DGSA results reveals that the TEM method provides reliable information close to the surface that permits an interpretation of the ice geometry and depth to the bedrock. Fig. 10 shows inversion results for TEM data collected at an ice glacier, yet we have no complimentary geophysical data available at this site. Our results are in agreement with those presented by Mudler et al. (2019) who obtained a range of relaxation time values from the CR method (10^{-4} s to 6×10^{-4} s) which is similar to the τ_ϕ values obtained from our TEM measurements (5×10^{-5} s). This supports the capability of the TEM method in a single-loop configuration to derive the high frequency polarization of ice. Furthermore, we observe that ϕ_{max}, τ_ϕ and c are in a similar range as Grombacher et al. (2021), yet a quantitative comparison is limited by a higher fluid salinity at their investigated antarctic site, compared to our alpine ice glacier. Mudler et al. (2019) used a different mathematical Cole-Cole model requiring five parameters to describe the frequency dependence of the complex electrical permittivity of frozen subsurface materials. In comparison, the MPA model requires only four parameters permitting to decrease the non-uniqueness of the inversion by reducing the number of parameters, as well as increasing the sensitivity of the solved model parameters. The inclusion of the model deployed by Mudler et al. (2019) into our forward modeler is an open area of research but beyond the scope of this study.

6. Conclusion

We present novel open-source Python routines for modeling and inversion of TEM data to investigate IP effects. We focus on the single-

loop configuration, which can be easily applied in areas with difficult terrain, as it offers simplified field procedures compared to configurations that use separated transmitter and receiver loops. To model the frequency dependence of the complex resistivity, we use the maximum phase angle model. We evaluated the capabilities of modeling and inversion routines developed for this study using both numerical and field data from three distinct case studies: 1) conductive, layered media without IP effects in a soda lake, 2) conductive, layered media with IP effects in a former graphite quarry, and 3) resistive, layered media with IP effects in an alpine ice glacier. In particular, this study demonstrates that the distance-based global sensitivity analysis (DGSA) is a suitable approach to assess the sensitivity of subsurface model parameters obtained from the inversion of TEM data with and without induced polarization (IP) effects. When compared with classical depth of investigation (DOI) approaches, DGSA results investigate a larger space of possible models and offer the advantage to quantify the individual sensitivity of model parameters. We demonstrate, using DGSA, that layered media without IP effects may show a decrease in model parameter sensitivity above the DOI. Our results show that the sensitivity of the inverted layer resistivity is generally higher than the sensitivity of the layer thickness. DGSA results from models retrieved using TEM data exhibiting IP effects reveal that the maximum phase angle is more influential than the relaxation time and the dispersion coefficient. Although our forward modeler was formulated specifically for the TEM-FAST 48 instrument in a single-loop configuration, our approach can be easily expanded to other instruments and additional configurations in the future. Our forward modeler may be used in future studies for survey design, as well as to stochastically assess the actual uncertainty of the estimated model parameters by means of Markov-chain Monte Carlo methods or Bayesian approaches.

CRediT authorship contribution statement

Lukas Aigner: Writing – review & editing, Writing – original draft, Visualization, Validation, Software, Methodology, Investigation, Formal analysis, Data curation, Conceptualization. **Dieter Werthmüller:** Writing – review & editing, Software, Methodology, Conceptualization. **Adrián Flores Orozco:** Writing – review & editing, Validation, Supervision, Resources, Project administration, Methodology, Investigation, Conceptualization.

Declaration of competing interest

The authors declare that they have no known competing financial interests or personal relationships that could have appeared to influence the work reported in this paper.

Data availability

All data and Python routines associated with this study are available open-source to facilitate full reproducibility of the results on github (https://github.com/aignerlukas/TEMIP_sensitivity) and on zenodo (https://zenodo.org/doi/10.5281/zenodo.10812429).

Acknowledgements

Appendix A. Appendix

A.1. TEM-FAST 48 system parameters

Table A1 shows the TEM-FAST system parameters that are used to parameterize the forward modeler. The TEM-FAST system allows injecting transmitter currents of 1 A or 4 A and the voltage decay can be measured in up to 48 logarithmically distributed time windows ranging from 4 μs to 16 ms. The transmitter current has a trapezoidal shape, where the front ramp is constant at 30 μs and the width of the current pulse ranges between 0.23 ms and 67.50 ms.

Table A1
Overview of the TEM-FAST 48 system parameters controlled by the time-key parameter for the 50 Hz filter including the last measured time window $t_{\max}$, the number of active time windows to measure the transient data n_{win}, the duration of the current pulse t_{on}, the off-time in between consecutive pulses t_{off} and the number of analog stacks n_{as}.

Setting	$t_{\max}$ (ms)	n_{win}	t_{on} (ms)	t_{off} (ms)	n_{as}
1	0.064	16	0.23	0.08	1024
2	0.128	20	0.47	0.16	512
3	0.256	24	0.94	0.31	256
4	0.512	28	1.88	0.63	128
5	1.024	32	3.75	1.25	64
6	2.048	36	7.50	2.50	32
7	4.096	40	22.50	7.50	16
8	8.192	44	37.50	12.50	8
9	16.384	48	67.50	22.50	4

The transmitter current decays over a finite time, which is commonly referred to as the turn-off ramp (t_r). The duration of t_r increases with the loop size affecting mainly the first readings and is therefore an essential parameter to correctly model the near-surface electrical resistivity (e.g., Raiche, 1984; Fitterman and Anderson, 1987; Zeng et al., 2019). Although t_r is pre-defined by the TEM-FAST system from the injected current and the loop size, Aigner et al. (2021) have shown that the actual length of t_r may be significantly shorter and depend on the injected current and the loop antenna size. We follow their approach to measure the correct length of t_r and an overview of the derived ramp data for all three sites are shown in Table A2.

Table A2
Overview of the TEM-FAST 48 turn-off ramp (t_r) data measured at the three field sites using a transmitter current of 4 A.

Side length (m)	Sodalakes t_r (us)	Graphite deposit t_r (us)	Ice glacier t_r (us)
6.25	0.45	0.48	–
12.50	0.95	0.98	–
25.00	1.50	–	2.70
50.00	4.30	–	5.10

A.2. Comparison to the proposed forward modeling routines to existing open-source and commercial algorithms

We investigate the performance and accuracy of our forward solver by comparing the modelled data to the commercial algorithm ZondTEM (Kaminsky, 2001) and the open-source algorithm SimPEG. Initially, we test the modelled data from the soda lake case study (conductive media without IP effect, shown in Table 1 using a 12.5 m and 50.0 m loop. Fig. A1 shows that our forward solver is basically equivalent for all 4 investigated test scenarios at times larger than approximately 20 μs. In particular, we can observe an rRMSE < 4% in the 12.5 m loop comparison to ZondTEM as well as in the 50.0 m loop comparison to SimPEG. However, the comparison to SimPEG for the 12.5 m loop (Fig. A1c) shows lower voltage readings in the first 5 time gates (< 10 μs). Fig. A1b shows a significantly different shape in the early time (< 9 μs) voltage readings, that might be attributed to the receiver loop being approximated by a vertical dipole in our case, whereas the algorithm of the ZondTEM software models the full receiver loop using multiple bipoles (Alex Kaminsky, ZondTEM, personal communication).
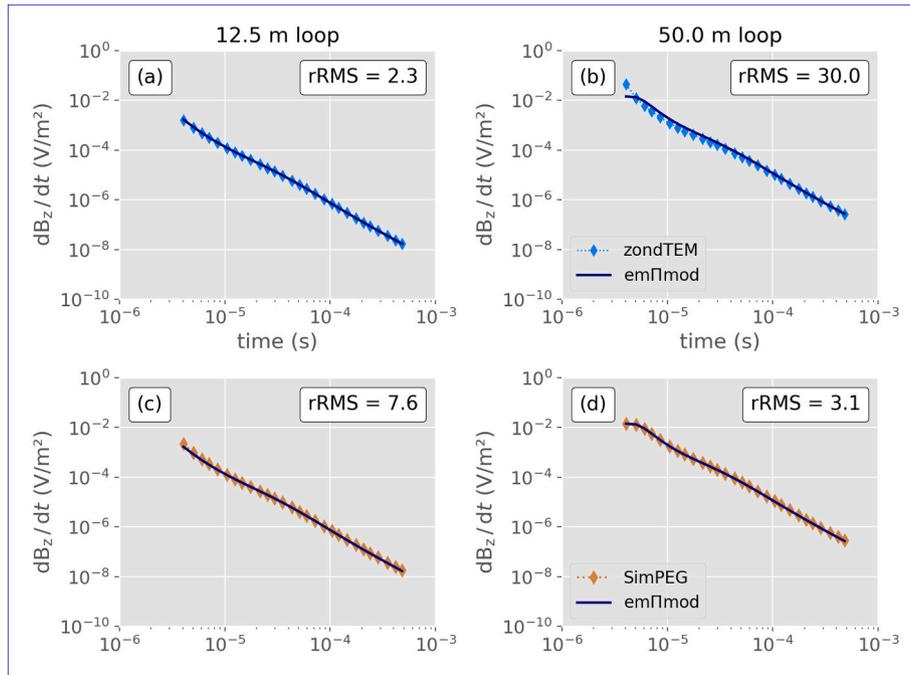
Fig. A1. Comparison between the empymod forward response of the soda lakes example (see Table 0) with the responses from ZondTEM (a) and (b), as well as with SimPEG (c) and (d).

Fig. A2 shows the comparison of the investigated model including IP-effects in the first layer. In general, we observe much larger misfits between the commercial algorithm and our implementation, yet the overall shape of the signals are similar. The comparisons for the 12.5 m loop in Fig. A2a, Fig. A2c and Fig. A2e show significantly lower rRMS values than the comparisons of the 50.0 m loop. The quality of the fit between the readings that are affected by a sign-reversal shows a similar pattern; better fit for the smaller loop and worse fit for the larger loop. The worst fit is clearly obtained for the 50.0 m loop in the case of $\oplus$IP in the graphite test case. Additionally, Fig. A2f shows a shift to earlier times of the first negative voltage reading by almost $10\,\mu s$ for our TEM-FAST forward solver.
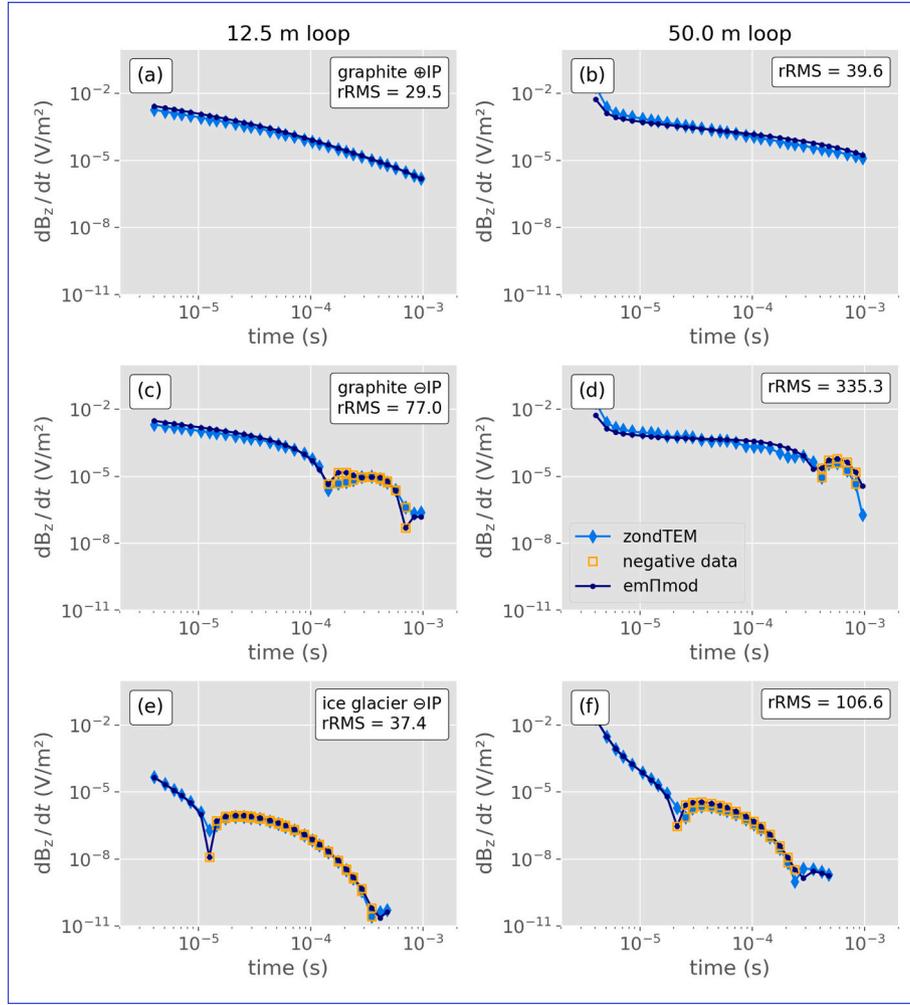
Fig. A2. Comparison of the empymod forward responses affected by the IP-effect to the responses from ZondTEM. (a) and (b) show the responses from the graphite example with a τ_ϕ of 50 ms which results in the positive IP-effect ($\oplus$IP). (c) and (d) show the responses from the graphite example with a τ_ϕ of 0.5 ms which results in the negative IP-effect ($\ominus$ IP). (e) and (f) show the responses from the ice glacier example.

A.3. Inversion: convergence parameters

Eq. (7) shows the relative root-mean-square error (rRMSE):

$$rRMSE = \sqrt{\frac{1}{n} \sum_{i=1}^{n} \left(\frac{d_{o,i} - d_{c,i}}{d_{m,i}} \right)^2} \tag{7}$$

with n being the number of voltage readings in the data vector, $d_{o,i}$ the observed data in (V/m^2) of the i-th reading and $d_{c,i}$ the calculated data (i.e., the model response) in (V/m^2) of the i-th voltage reading. Eq. (8) shows the error-weighted root-mean-square error (χ^2):

$$\chi^2 = \sqrt{\frac{1}{n} \sum_{i=1}^{n} \left(\frac{d_{o,i} - d_{c,i}}{\varepsilon_i} \right)^2} \tag{8}$$

with the same parameters as above adding only the being the absolute data error (ε_i) in (V/m^2) of the i-th voltage reading.

A.4. Data fit for case studies associated to polarizable media in graphite-rich and glacier sites

Fig. A3 shows that the developed inversion algorithm is capable of fitting the measured field data that show a $\oplus$IP effect as we do not observe any negative voltage readings.
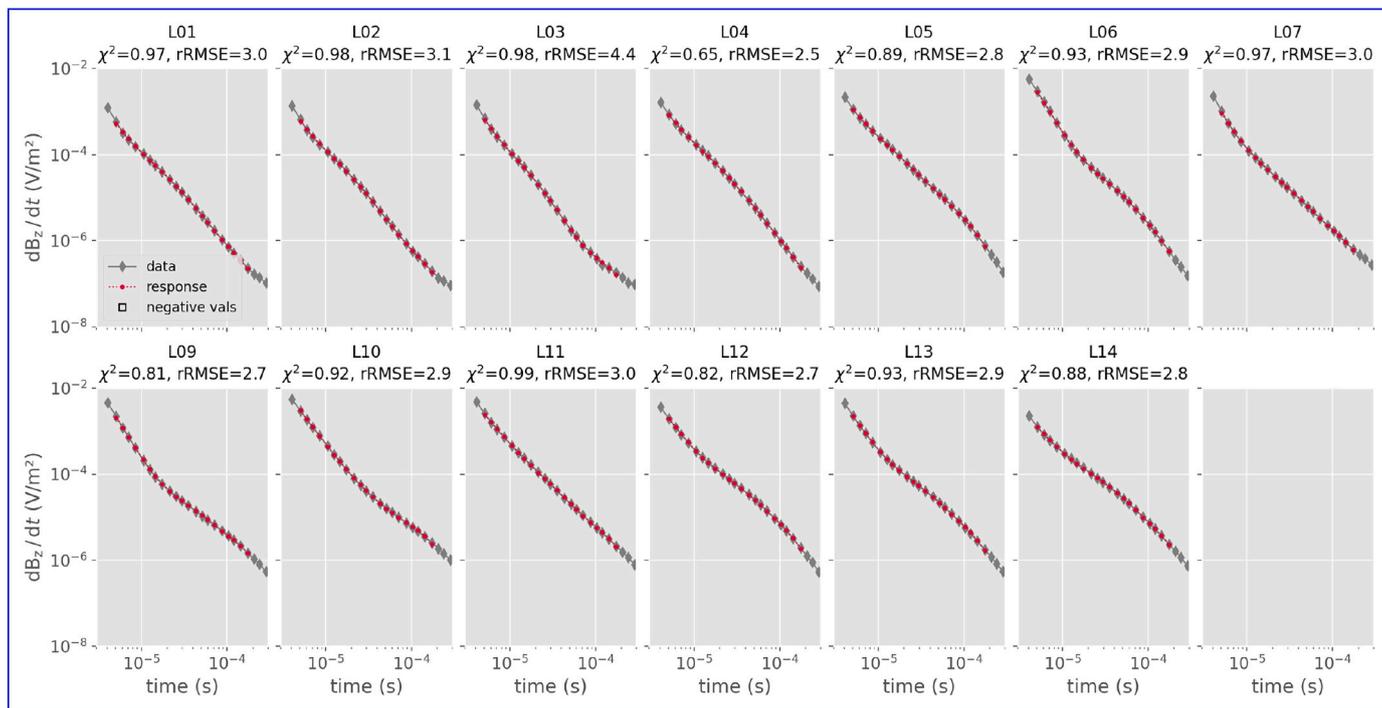
Fig. A3. Data fit of the field example at the graphite deposit for all TEM inversion results shown in Fig. 6.

Fig. A4 shows that the inversion fits the measured field data that show a ⊖ IP effect as we observe negative voltage readings starting at the 12th reading at ca. 23 µs.
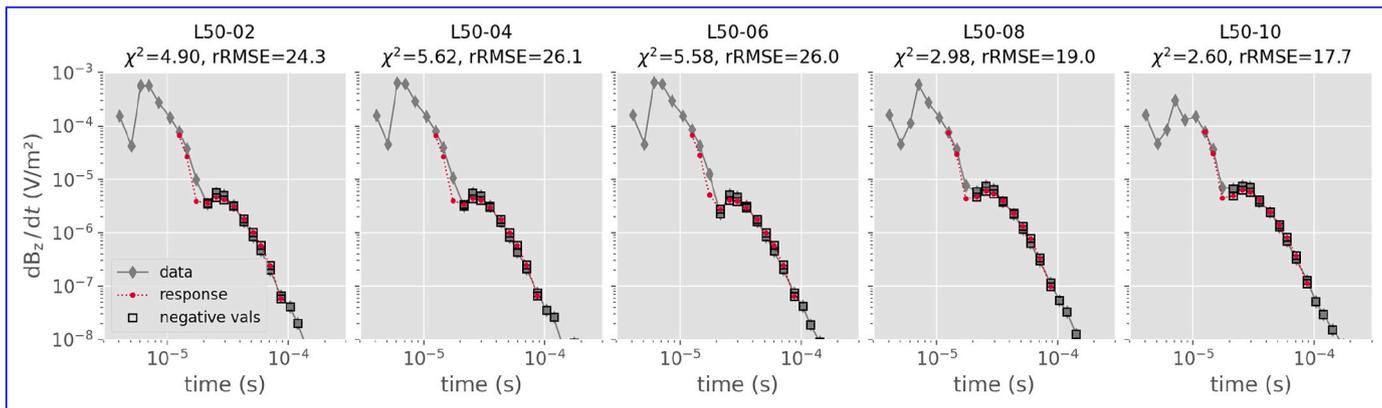
Fig. A4. Data fit of the field example at the ice glacier for all TEM inversion results shown in Fig. 10.

References

Abdulsamad, F., Revil, A., Ghorbani, A., Toy, V., Kirilova, M., Coperey, A., Duvillard, P. A., Ménard, G., Ravanel, Ludovic, 2019. Complex conductivity of graphitic schists and sandstones. J. Geophys. Res. Solid Earth 124 (8), 8223–8249. https://doi.org/10.1029/2019JB017628.

Aigner, Lukas, Högenauer, Philipp, Bücker, Matthias, Orozco, Adrián Flores, 2021. A flexible single loop setup for water-borne transient electromagnetic sounding applications. Sensors 21 (19), 6624. https://doi.org/10.3390/s21196624.

Auken, Esben, Christiansen, Anders Vest, 2004. Layered and laterally constrained 2D inversion of resistivity data. Geophysics 69 (3), 752–761.

Auken, Esben, Christiansen, Anders Vest, Kirkegaard, Casper, Fiandaca, Gianluca, Schamper, Cyril, Behroozmand, Ahmad Ali, Binley, Andrew, Nielsen, Emil, Effersø, Flemming, Christensen, Niels Bøie, et al., 2015. An overview of a highly versatile forward and stable inverse algorithm for airborne, ground-based and borehole electromagnetic and electric data. Explor. Geophys. 46 (3), 223–235.

Bérubé, Charles L., Chouteau, Michel, Shamsipour, Pejman, Enkin, Randolph J., Olivo, Gema R., 2017. Bayesian inference of spectral induced polarization

parameters for laboratory complex resistivity measurements of rocks and soils. Comput. Geosci. 105, 51–64. https://doi.org/10.1016/j.cageo.2017.05.001.

Bücker, Matthias, Orozco, Adrián Flores, Kemna, Andreas, 2018. Electrochemical polarization around metallic particles—part 1: the role of diffuse-layer and volume-diffusion relaxation. Geophysics 83 (4), E203–E217. https://doi.org/10.1190/geo2017-0401.1.

Bücker, Matthias, Orozco, Adrián Flores, Gallistl, Jakob, Steiner, Matthias, Aigner, Lukas, Hoppenbrock, Johannes, Glebe, Ruth, Barrera, Wendy Morales, de la Paz, Carlos Pita, García, César Emilio García, et al., 2021. Integrated land and water-borne geophysical surveys shed light on the sudden drying of large karst lakes in southern Mexico. Solid Earth 12 (2), 439–461.

Butterworth, Stephen, 1930. On the theory of filter amplifiers. Wireless Eng. 7 (6), 536–541.

Christiansen, Anders Vest, Auken, Esben, 2012. A global measure for depth of investigation. Geophysics 77 (4), WB171–WB177.

Christiansen, Anders Vest, Auken, Esben, Sprensen, Kurt, 2006. The transient electromagnetic method. In: Groundwater Geophysics. Springer, pp. 179–225.

Cockett, Rowan, Kang, Seogi, Heagy, Lindsey J., Pidlisecky, Adam, Oldenburg, Douglas W., 2015. Sim-PEG: an open source framework for simulation and gradient based

parameter estimation in geophysical applications. Comput. Geosci. 85, 142–154. https://doi.org/10.1016/j.cageo.2015.09.015.

Fenwick, Darryl, Scheidt, Céline, Caers, Jef, 2014. Quantifying asymmetric parameter interactions in sensitivity analysis: application to reservoir modeling. Math. Geosci. 46 (4), 493–511. https://doi.org/10.1007/s11004-014-9530-5.

Fiandaca, G., Christiansen, A.V., Auken, E., 2015. Depth of investigation for multi-parameters inversions. In: Near Surface Geoscience 2015-21st European Meeting of Environmental and Engineering Geophysics, 2015.1. EAGE Publications BV, pp. 1–5. https://doi.org/10.3997/2214-4609.201413797.

Fiandaca, Gianluca, Madsen, Line Meldgaard, Maurya, Pradip Kumar, 2018. Re-parameterisations of the Cole–Cole model for improved spectral inversion of induced polarization data. Near Surface Geophys. 16 (4), 385–399.

Fitterman, David V., Anderson, Walter L., 1987. Effect of transmitter turn-off time on transient soundings. Geoexploration 24 (2), 131–146.

Flores Orozco, Adrián, Williams, Kenneth H., Long, Philip E., Hubbard, Susan S., Kemna, Andreas, 2011. Using complex resistivity imaging to infer biogeochemical processes associated with bioremediation of an uranium-contaminated aquifer. J. Geophys. Res. Biogeosci. 116, G3. https://doi.org/10.1029/2010JG001591.

Flores Orozco, Adrián, Kemna, Andreas, Zimmermann, Egon, 2012. Data error quantification in spectral induced polarization imaging. Geophysics 77 (3), E227–E237. https://doi.org/10.1190/geo2010-0194.1.

Flores Orozco, Adrián, Lukas, Aigner, Gallistl, Jakob, 2021. Investigation of cable effects in spectral induced polarization imaging at the field scale using multicore and coaxial cables. Geophysics 86 (1), E59–E75. doi:10.1190/geo2019-0552.1.

Flores, Carlos, Peralta-Ortega, Sergio A., 2009. Induced polarization with in-loop transient electromagnetic soundings: a case study of mineral discrimination at El Arco porphyry copper, Mexico. J. Appl. Geophys. 68 (3), 423–436.

Glover, P.W.J., 2015. 11.04–Geophysical properties of the near surface earth: electrical properties. In: Treatise on Geophysics, pp. 89–137. https://doi.org/10.1016/B978-0-444-53802-4.00189-5.

Grombacher, Denys, Auken, Esben, Foged, Nikolaj, Bording, Thue, Foley, Neil, Doran, Peter T., Mikucki, Jill, Dugan, Hilary A., Garza-Giron, Ricardo, Myers, Krista, Virginia, Ross A., Tulaczyk, Slawek, May 2021. Induced polarization effects in airborne transient electromagnetic data collected in the McMurdo Dry Valleys, Antarctica. J. Int. 226 (3), 1574–1583 issn: 0956-540X. https://doi.org/10.1093/gji/ggab148. eprint: https://academic.oup.com/gji/article/226/3/1574/38270582/ggab148.pdf. url: https://doi.org/10.1093/gji/ggab148.

Günther, T., Müller-Petke, M., 2012. Hydraulic properties at the North Sea island of Borkum derived from joint inversion of magnetic resonance and electrical resistivity soundings. Hydrol. Earth Syst. Sci. 16 (9), 3279–3291.

Heagy, Lindsey J., Cockett, Rowan, Kang, Seogi, Rosenkjaer, Gudni K., Oldenburg, Douglas W., 2017. A framework for simulation and inversion in electromagnetics. Comput. Geosci. 107, 1–19. https://doi.org/10.1016/j.cageo.2017.06.018.

Herman, Jon, Usher, Will, Jan. 2017. SALib: an open-source Python library for Sensitivity Analysis. J. Open Source Softw. 2 (9) https://doi.org/10.21105/joss.00097.

Hermans, Thomas, Nguyen, Frédéric, Klepikova, Maria, Dassargues, Alain, Caers, Jef, 2018. Uncertainty quantification of medium-term heat storage from short-term geophysical experiments using Bayesian evidential learning. Water Resour. Res. 54 (4), 2931–2948. https://doi.org/10.1002/2017WR022135.

Hunziker, Jürg, Thorbecke, Jan, Slob, Evert, 2015. The electromagnetic response in a layered vertical transverse isotropic medium: a new look at an old problem. Geophysics 80 (1), F1–F18. https://doi.org/10.1190/geo2013-0411.1.

Inman, Joseph Robert, 1975. Resistivity inversion with ridge regression. Geophysics 40 (5), 798–817.

Iwanaga, Takuya, Usher, William, Herman, Jonathan, May 2022. Toward SALib 2.0: Advancing the accessibility and interpretability of global sensitivity analyses. Socio-Environ. Syst. Model. 4, 18155. https://doi.org/10.18174/sesmo.18155. https://sesmo.org/article/view/18155.

Kaminsky, Alex, 2001. ZondTEMID (Zond Software corporation). Version 28092019. url: http://zond-geo.com/english/zond-software/electromagnetic-sounding/zondtem1d/.

Kang, Seogi, Oldenburg, Douglas W., 2016. On recovering distributed IP information from inductive source time domain electromagnetic data. Geophys. J. Int. 207 (1), 174–196.

Kang, Seogi, Oldenburg, Douglas W., Heagy, Lindsey J., 2020. Detecting induced polarisation effects in time-domain data: a modelling study using stretched exponentials. Explor. Geophys. 51 (1), 122–133. https://doi.org/10.1080/08123985.2019.1690393.

Kemna, Andreas, 2000. Tomographic Inversion of Complex Resistivity: Theory and Application. Der Andere Verlag.

Key, Kerry, 2009. 1D inversion of multicomponent, multifrequency marine CSEM data: Methodology and synthetic studies for resolving thin resistive layers. Geophysics 74 (2), F9–F20. https://doi.org/10.1190/1.3058434.

Key, Kerry, 2012. Is the fast Hankel transform faster than quadrature? Geophysics 77 (3), F21–F30. https://doi.org/10.1190/geo2011-0237.1.

Kozhevnikov, N.O., Antonov, E.Yu., 2012. Fast-decaying inductively induced polarization in frozen ground: a synthesis of results and models. J. Appl. Geophys. 82, 171–183 issn: 0926-9851. https://doi.org/10.1016/j.jappgeo.2012.03.008.

Lee, T., 1975. Sign reversals in the transient method of electrical prospecting (one-loop version). Geophys. Prospect. 23 (4), 653–662. https://doi.org/10.1111/j.1365-2478.1980.tb01247.x.

Li, Jianhui, Farquharson, Colin G., Xiangyun, Hu, 2017. 3D vector finite-element electromagnetic forward modeling for large loop sources using a total-field algorithm and unstructured tetrahedral grids. Geophysics 82 (1), E1–E16. https://doi.org/10.1190/geo2016-0004.1.

Lin, Changhong, Fiandaca, Gianluca, Auken, Esben, Couto, Marco Antonio, Christiansen, Anders Vest, 2019. A discussion of 2D induced polarization effects in airborne electromagnetic and inversion with a robust 1D laterally constrained inversion scheme. Geophysics 84 (2), E75–E88.

Madsen, Line Meldgaard, Fiandaca, Gianluca, Auken, Esben, Christiansen, Anders Vest, Aug. 2017. Timedomain induced polarization – an analysis of Cole–Cole parameter resolution and correlation using Markov Chain Monte Carlo inversion. Geophys. J. Int. 211 (3), 1341–1353. issn: 0956-540X. https://doi.org/10.1093/gji/ggx355. eprint. https://academic.oup.com/gji/article-pdf/211/3/1341/20938328/ggx355.pdf.

Maierhofer, Theresa, Hauck, Christian, Hilbich, Christin, Kemna, Andreas, Flores-Orozco, Adrián, 2022. Spectral induced polarization imaging to investigate an ice-rich mountain permafrost site in Switzerland. Cryosphere 16 (5), 1903–1925. https://doi.org/10.5194/tc-16-1903-2022.

Marquardt, Donald W., 1963. An algorithm for least-squares estimation of nonlinear parameters. J. Soc. Ind. Appl. Math. 11 (2), 431–441.

Maurya, Pradip Kumar, Grombacher, Denys, Lind, Johan, Lane, John W., Auken, Esben, 2022. Inversion of induced polarization-affected towed-transient electromagnetic data in a lateritic regolith geology: a case study from western Tanzania. Geophysics 87 (4), B247–B254.

Michel, Hadrien, Nguyen, Frédéric, Kremer, Thomas, Elen, Ann, Hermans, Thomas, 2020. 1D geological imaging of the subsurface from geophysical data with Bayesian Evidential Learning. Comput. Geosci. 138, 104456 https://doi.org/10.1016/j.cageo.2020.104456.

Mudler, Jan, Hördt, Andreas, Przyklenk, Anita, Fiandaca, Gianluca, Maurya, Pradip Kumar, Hauck, Christian, 2019. Two-dimensional inversion of wideband spectral data from the capacitively coupled resistivity method – first applications in periglacial environments. Cryosphere 13 (9), 2439–2456. https://doi.org/10.5194/tc-13-2439-2019.

Nabighian, Misac N., 1979. Quasi-static transient response of a conducting half-space—an approximate representation. Geophysics 44 (10), 1700–1705.

Nabighian, Misac N., Macnae, James C., et al., 1991. Time domain electromagnetic prospecting methods. In: Electromagnetic Methods in Applied Geophysics, 2 Part A, pp. 427–509.

Osterman, Gordon, Sugand, Madhuri, Keating, Kristina, Binley, Andrew, Slater, Lee, 2019. Effect of clay content and distribution on hydraulic and geophysical properties of synthetic sand-clay mixtures. Geophysics 84 (4), E239–E253. https://doi.org/10.1190/geo2018-0387.1.

Paige, Christopher C., Saunders, Michael A., 1982. LSQR: an algorithm for sparse linear equations and sparse least squares. ACM Trans. Math. Softw. (TOMS) 8 (1), 43–71.

Pelton, W.H., Ward, S.H., Hallof, P.G., Sill, W.R., Hi Nelson, P., 1978. Mineral discrimination and removal of inductive coupling with multifrequency IP. Geophysics 43 (3), 588–609. https://doi.org/10.1190/1.1440839.

Perzan, Z., Babey, T., Caers, J., Bargar, J.R., Maher, K., 2021. Local and Global Sensitivity Analysis of a Reactive Transport Model Simulating Floodplain Redox Cycling. Water Resour. Res. 57 (12), e2021WR029723 https://doi.org/10.1029/2021WR029723.

Raiche, A.P., 1984. The effect of ramp function turn-off on the TEM response of layered earth. Explor. Geophys. 15 (1), 37–41.

Revil, A., Glover, P.W.J., 1998. Nature of surface electrical conductivity in natural sands, sandstones, and clays. Geophys. Res. Lett. 25 (5), 691–694. https://doi.org/10.1029/98GL00296.

Revil, André, Mao, Deqiang, Shao, Zhenlu, Sleevi, Michael F., Wang, Deming, 2017. Induced polarization response of porous media with metallic particles—part 6: the case of metals and semimetals. Geophysics 82 (2), E97–E110. https://doi.org/10.1190/geo2016-0389.1.

Rousseeuw, Peter J., 1987. Silhouettes: a graphical aid to the interpretation and validation of cluster analysis. J. Comput. Appl. Math. 20, 53–65. https://doi.org/10.1016/0377-0427(87)90125-7.

Rücker, Carsten, Günther, Thomas, Wagner, Florian M., 2017. pyGIMLi: An open-source library for modelling and inversion in geophysics. Comput. Geosci. 109, 106–123. issn: 0098–3004. https://doi.org/10.1016/j.cageo.2017.07.011. url: http://www.sciencedirect.com/science/article/pii/S0098300417300584.

Saltelli, Andrea, Ratto, Marco, Andres, Terry, Campolongo, Francesca, Cariboni, Jessica, Gatelli, Debora, Saisana, Michaela, Tarantola, Stefano, 2008. Global Sensitivity Analysis: The Primer. John Wiley & Sons.

Schnabel, W., Krenmayer, H.G., Linner, M., 2012. Geologische Karte der Republik Österreich 1:50000, Blatt 55 Ober-Grafendorf. https://doi.org/10.24341/tethys.28.

Seidel, Marc, Tezkan, Bülent, 2017. 1D Cole-Cole inversion of TEM transients influenced by induced polarization. J. Appl. Geophys. 138, 220–232. issn: 0926-9851. https://doi.org/10.1016/j.jappgeo.2017.01.011.

Smith, Richard S., West, G.F., 1988. Inductive interaction between polarizable conductors: an explanation of a negative coincident-loop transient electromagnetic response. Geophysics 53 (5), 677–690.

Spear, R.C., Hornberger, G.M., 1980. Eutrophication in peel inlet—II. Identification of critical uncertainties via generalized sensitivity analysis. Water Res. 14 (1), 43–49. issn: 0043–1354. https://doi.org/10.1016/0043-1354(80)90040-8. url. https://www.sciencedirect.com/science/article/pii/0043135480900408.

Spies, Brian R., 1980. A field occurrence of sign reversals with the transient electromagnetic method. Geophys. Prospect. 28 (4), 620–632. https://doi.org/10.1111/j.1365-2478.1975.tb01551.x.

Spies, Brian R., 1989. Depth of investigation in electromagnetic sounding methods. Geophysics 54 (7), 872–888.

Telford, William Murray, Telford, W.M., Geldart, L.P., Sheriff, Robert E., Sheriff, R.E., 1990. Applied Geophysics, vol. 1. Cambridge University Press.

Viezzoli, Andrea, Manca, Giovanni, 2020. On airborne IP effects in standard AEM systems: Tightening model space with data space. Explor. Geophys. 51 (1), 155–169. https://doi.org/10.1080/08123985.2019.1681895.

Wagner, F.M., Mollaret, C., Günther, T., Kemna, A., Hauck, C., Sept. 2019. Quantitative imaging of water, ice and air in permafrost systems through petrophysical joint inversion of seismic refraction and electrical resistivity data. Geophys. J. Int. 219 (3), 1866–1875. https://doi.org/10.1093/gji/ggz402.

Weidelt, P., 1982. Response characteristics of coincident loop transient electromagnetic systems. Geophysics 47 (9), 1325–1330. https://doi.org/10.1190/1.1441393.

Weller, Andreas, Slater, Lee, Binley, Andrew, Nordsiek, Sven, Shujie, Xu, 2015. Permeability prediction based on induced polarization: Insights from measurements on sandstone and unconsolidated samples spanning a wide permeability range. Geophysics 80 (2), D161–D173. https://doi.org/10.1190/geo2014-0368.1.

Werthmüller, Dieter, 2017. An open-source full 3D electromagnetic modeler for 1D VTI media in Python: empymod. Geophysics 82 (6), WB9–WB19. https://doi.org/10.1190/geo2016-0626.1.

Werthmüller, Dieter, Key, Kerry, Slob, Evert C., 2019. A tool for designing digital filters for the Hankel and Fourier transforms in potential, diffusive, and wavefield modelingDigital filter designing tool. Geophysics 84 (2), F47–F56. https://doi.org/10.1190/geo2018-0069.1.

Yogeshwar, Pritam, Küpper, Mira, Tezkan, Bülent, Rath, Volker, Kiyan, Duygu, Byrdina, Svetlana, Cruz, José, Andrade, César, Viveiros, Fatima, 2020. Innovative boat-towed transient electromagnetics—investigation of the Furnas volcanic lake hydrothermal system, Azores. Geophysics 85 (2), E41–E56.

Zeng, Sihong, Xiangyun, Hu, Li, Jianhui, Farquharson, Colin G., Wood, Peter C., Xushan, Lu, Peng, Ronghua, 2019. Effects of full transmitting-current waveforms on transient electromagnetics: Insights from modeling the Albany graphite deposit. Geophysics 84 (4), E255–E268. https://doi.org/10.1190/geo2018-0573.1.